Chapter 1

Introduction

1.1 The Standard Model

A physics model is a description of a system using physics and mathematical concepts and language. Standard Model (SM) is a physics model that summarizes what is currently known about the subatomic world. The SM is composed of two gauge symmetry theories: the Glashow-Salam-Weinberg Model (GSW) [1–3] describing electroweak interactions; the Quantum Chromodynamics (QCD) [4] describing the strong interactions. In SM, there are two types of fundamental particles, fermions and bosons. Fermions are the building block of matter, and bosons are the intermediate particles of the four fundamental interactions of SM, i.e., strong, weak, electromagnetic and gravitational force. In this chapter, we briefly introduce the components of the SM and the related theories to this thesis.

1.1.1 Fundamental particles

Fermions are defined as particles with half integer spin (intrinsic angular momentum), like leptons, quarks, proton, etc, while bosons are particles with integer spin, like the photon and the Higgs boson. The fundamental particles of SM are shown in Figure 1.1.
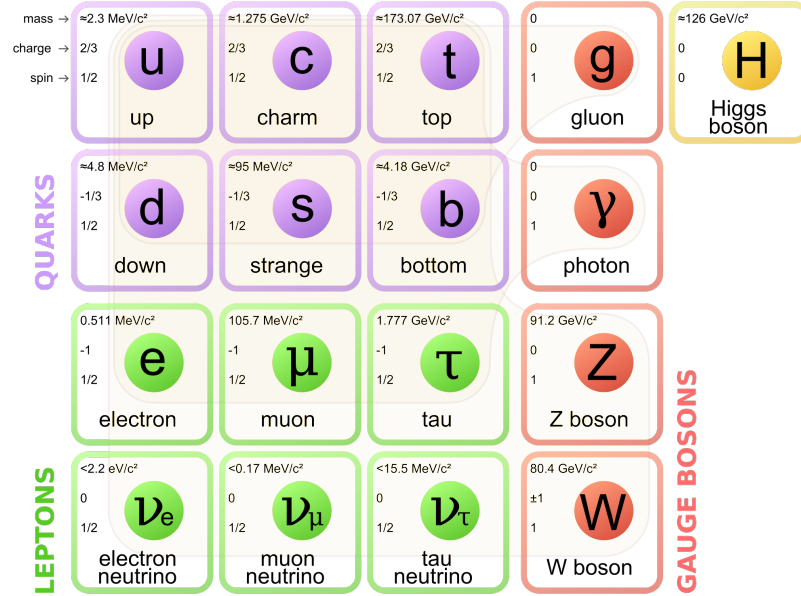

Figure 1.1: Standard model of elementary particles: the 12 fundamental fermions and 5 fundamental bosons. [5]

Quarks

In SM, there are six flavors of quarks: up (u), down (d), strange (s), charm (c), top (t), and bottom (b). Quarks carry properties like flavor, color, spin, charge, mass, etc. All quarks have spin $\frac{1}{2}$ in SM and they belong to one of the three generations: u and d quarks belong to the first generation; s and c quarks are the second generation quarks; t and b quarks make up the third generation. The color is a property of

particle. In Quantum Chromodynamics, color is conserved in strong interactions. There are normally 3 types of color: red, blue, green. A particle is colorless if it carries a net color charge of zero.

Leptons

Leptons are fundamental particles, which are also fermions. As shown in Figure 1.1, there are three generation of leptons: electron (e) and electron neutrino (ν_e) are the first generation; muon (μ) and muon neutrino (ν_μ) are the second generation; tau (τ) and tau neutrino (ν_τ) are the third generation. Leptons have electronic charge, but do not carry color charges. Thus they are involved in the electroweak interactions, but not the strong interactions.

Bosons

Every interaction has its mediator: the photon (γ) for electromagnetic force, W and Z boson for weak force, gluon (g) for strong force and graviton (not found yet) for gravity. Higgs boson (H), although not a mediator, accounts for the mass of other fundamental particles, which will be elaborated in the following section. The W, Z, γ and g bosons having spin 1, are called vector boson. H boson has spin 0, which is called a scaler boson. There are two W bosons, distinguished by their electron charges, W^+ and W^-.

1.2 Fundamental interactions

In SM, there are four fundamental forces : strong, electromagnetic, weak and gravitational force, as shown in Table 1.1. The "Strength" column in Table 1.1 is not the real strength of the force, but a value to show the relative strength of these forces.

Since gravity is so small compared to other three forces, it is mostly not considered in the process of particle physics. The strong force is described by the Quantum Chromodynamics. And the electromagnetic force and weak force are unified into electroweak interaction, described by the Glashow-Weinberg-Salam (GSW) model. The theory of particular interest to this thesis is the Quantum Chromodynamics (QCD), which will be introduced in the following section.

Force	Strength	Mediator
Strong	10	Gluon
Electromagnetic	10^{-2}	Photon
Weak	10^{-13}	W and Z
Gravitational	10^{-42}	Graviton

Table 1.1: Summary of the four fundamental forces in Standard Model [6].

1.2.1 Quantum Electrodynamics (QED)

QED is the theory describing the electromagnetic interaction: the interaction between electric charged particles via the exchange of photons. The primitive process in QED, in the form of Feynman diagram, is shown in Figure 1.2. An electron comes in, and radiates a photon, then goes out. By connecting couple of these primitive processes together, we can get complex process like the one in Figure 1.3. In Figure 1.3, the electron and positron annihilate into a photon, which further decays to a pair of quarks, and then one of the two quarks radiates a gluon. The photon in Figure 1.3 is a virtual particle. Virtual particles are not observable, which are called "off-shell" particles. While real particles, in Figure 1.3, are the incoming electron and positron, and outgoing quarks and gluons, which can be observed and are "on-shell"

.

1.2.2 Quantum Chromodynamics (QCD) and jets

QCD is a theory describing the strong force and the involved fundamental particles. As we see from Table 1.1, strong force is the strongest force of the four. However, unlike the long range electromagnetic force, the strong force could only affect $\approx 10^{-15}$ m (1 fm), which is about the radius of a nucleus.

Color is one of the unique properties of QCD. The color of QCD is an analogy to the charge of QED. There are three types of colors charges: red, blue, green. Each
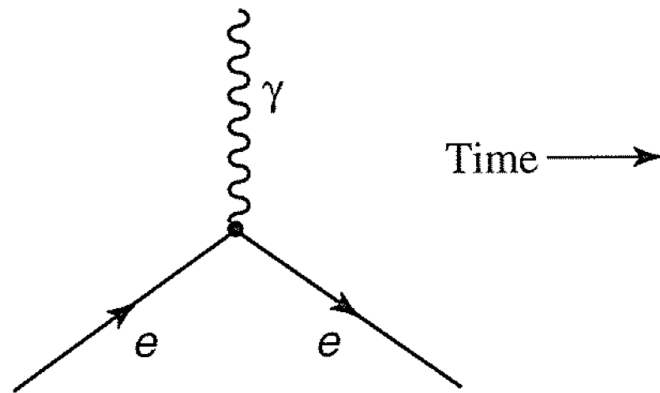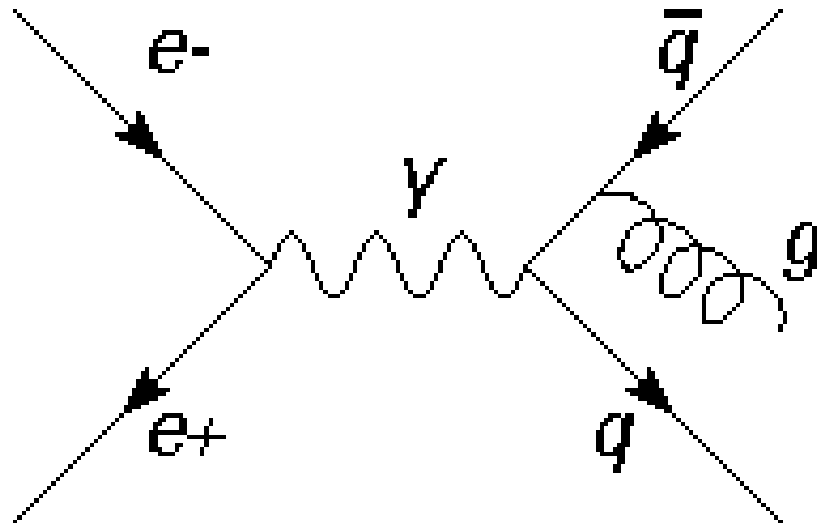
Figure 1.2: The primitive QED process in SM.

Figure 1.3: Feynman diagram for electron annihilation.

quark carry one kind of color. So, for example, there are three types of top quarks in QCD: the blue top quark, the green top quark, and the red top quark. This is the same for all the other five flavors of quarks. Anti-quark carries one kind of anti-color. Gluons is the boson intermediating the strong force, just like the photon is the mediator of the electromagnetic force. Gluons has a color and an anti-color. When two quarks interact with each other, they interact through a gluon by exchanging colors. For example, as shown in Figure 1.4, one red quark comes in, radiates a gluon with color red and anti-blue, and a blue quark goes out. In terms of the color SU(3) symmetry, there are 8 gluons in QCD, as shown in Equation 1.1.
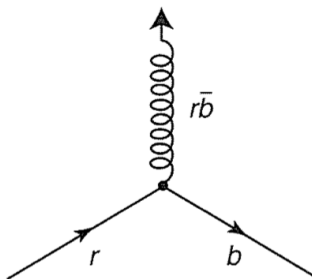

Figure 1.4: The illustration of quark-gluon interaction [6].

$$(r\bar{b} + b\bar{r})/\sqrt{2} \qquad -i(r\bar{g} - g\bar{r})/\sqrt{2}$$

$$-i(r\bar{b} - b\bar{r})/\sqrt{2} \qquad (b\bar{g} + g\bar{b})/\sqrt{2}$$

$$(r\bar{r} - b\bar{b})/\sqrt{2} \qquad -i(b\bar{g} - g\bar{b})/\sqrt{2} \qquad (1.1)$$

$$(r\bar{g} + g\bar{r})/\sqrt{2} \qquad (r\bar{r} + b\bar{b} - 2g\bar{g})/\sqrt{6}$$

Unlike charge particles, colored particle could not be free. What we see in experiments and daily life is color-singlet. So we can never observe a single quark or a single gluon in an experiment. What we observe is the hadronization product of quarks and gluons, which are called jets and introduced in the following text. The existence of quarks and gluons is proved by indirect experiments via jets. Here we will introduce the essential components of QCD.

The coupling constant

The coupling constant is a scaler quantity describing the strength of an interaction. Here in QCD, the coupling constant α_s is :

$$\alpha_s(|q^2|) = \frac{2\pi}{(11n - 2f)ln(|q^2|/\Lambda^2)} \quad (|q^2| \gg \Lambda^2) \qquad (1.2)$$

where $|q|^2$ is the squared energy-momentum 4-vector of the mediator gluon, n is the number of colors (3, in SM), f is the number of flavors (3, in SM), and Λ is a parameter determined from experimental data, which is in the range of 100~500 MeV.

Notice that α_s is not a constant. It is a function of $|q|^2$. Because of this, it is also named the "running coupling constant". The experimental measurements are shown in Figure 1.5.
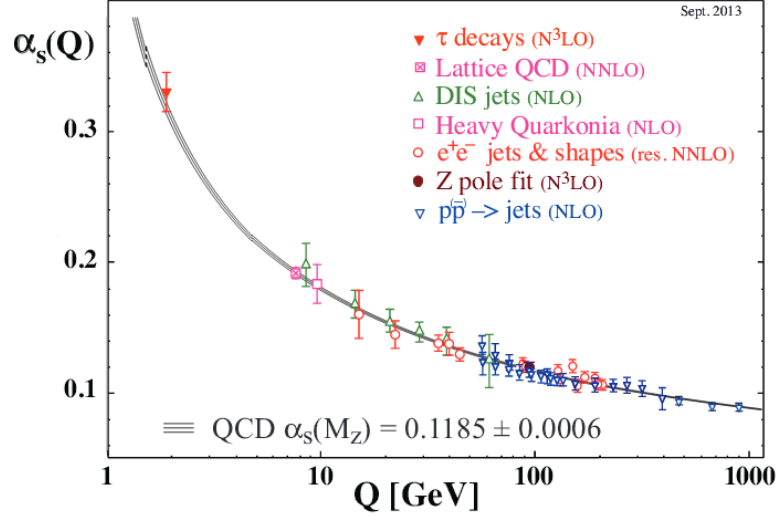

Figure 1.5: The running coupling constant of QCD. NLO is short for the next leading order. NNLO is short for next-next-leading order.

Asymptotic freedom

As we see from Equation 1.2, when $|q|^2$ increases, α_s decreases. At large $|q|^2$, corresponding to short distances ($\leq 1\ fm$), the strong force is so weak that quarks inside of proton travel freely. At very high energies, it is also possible to form quark-gluon plasma, since their interactions are so weak. This is called the asymptotic freedom.

QCD confinement

QCD confinement means that the force between quarks will hugely increase when they are separated. So one has to exert a lot energy to try to separate a quark from

other quarks. And this energy will become large enough for the mediator gluon to decay into a new quark pair. As illustrated in Figure 1.6, when the two charm quarks are pulled apart, the strong force between them increases, and the mediating gluon will have a large amount of energy. Before the charm quarks are further separated, the gluon creates a pair of $d\bar{d}$ quark pair. This process continues, and eventually the particle formed by $c\bar{c}$ quarks will become two particles each formed by c and d quarks. The gluon could create any pair of new quarks, as long as the energy is large enough to create them. Here we use $d\bar{d}$ quark pair as illustration. And also $d\bar{d}$ quark pair requires relatively low energy to create, compared to other quark anti-quark pairs.
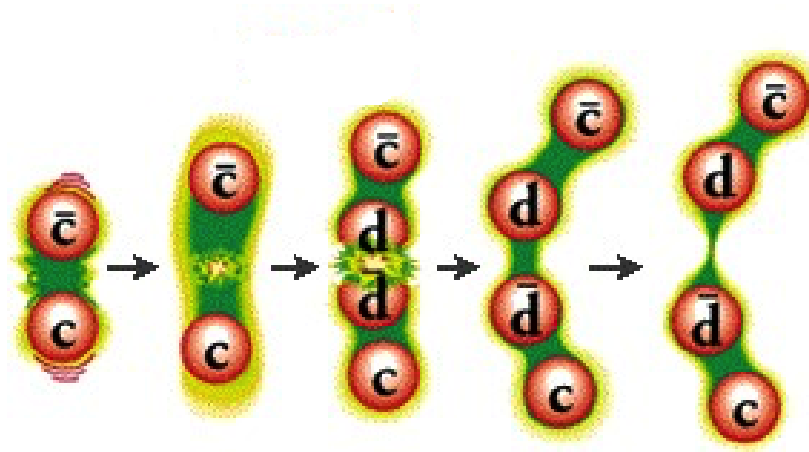

Figure 1.6: The illustration of QCD confinement [7].

Jet formation

When quarks and gluons are created in a high energy collision, they will move away from the collision position freely for a brief moment. And then, because of QCD confinement, when the quarks are separated by a distance $\geq 1fm$, new quarks

pairs are created from the virtual gluons exchanged by the interaction between the initial quarks, as shown in Figure 1.7. This process stops when the gluons or quarks don't have enough kinetic energy to create new quark-aniquark pairs. The quarks or gluons initially created by the the energetic collision, enentually become hadrons; this process is called hadronization. The stream of particles created by the hadronization of a single quark or gluon is called a jet, as shown in Figure 1.8.
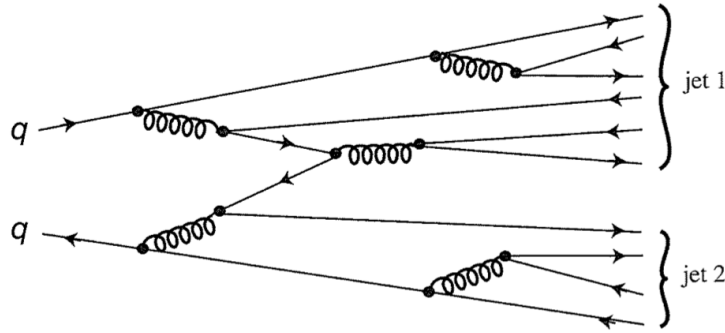

Figure 1.7: The hadronization process [6].

1.2.3 The SM Higgs mechanism

The Higgs boson is a scaler boson, with spin 0. In SM, Higgs has a non-zero vacuum expectation value (VEV), as shown in Figure 1.9, while all other particles have zero VEVs. As shown in Figure 1.9, the Higgs particle with the non-zero VEV
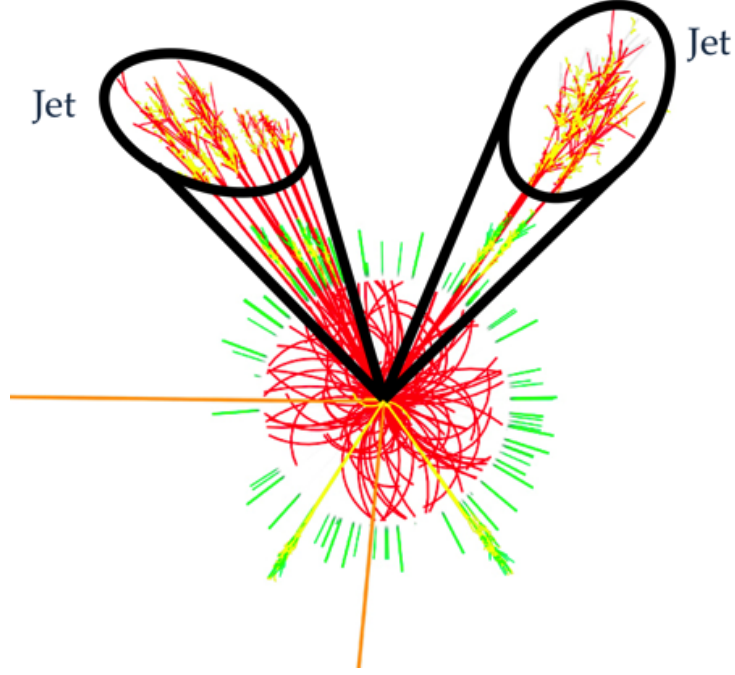
Figure 1.8: A sketch of jets formation in a high energy collision. Hadrons are clustered together to make jets.

is tending to slide down to the bottom of the potential. While the Higgs particle is on top of the potential, a rotation of the whole system in space-time dimensions, does not change its symmetry. However, when the Higgs particle is sliding off the potential to the bottom, as shown in Figure 1.9, the rotation symmetry is broken. This is called the spontaneous symmetry breaking. The Higgs field with non-zero VEV is permeating all the space. And fermions, by their interactions with the Higgs particle, gain their masses. The magnitude of a fermion's mass is proportional to the its coupling strength with the Higgs field.

The W^+, W^- and Z bosons gain their masses through the spontaneous electroweak symmetry breaking mechanism. In an unbroken unified electroweak theory, there are
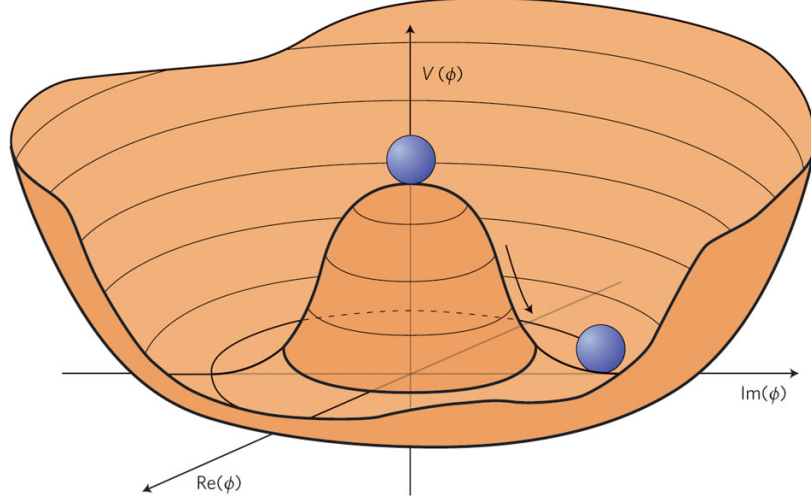
Figure 1.9: The non-zero vacuum potential of Higgs field. The $Im(\phi)$ and $Re(\phi)$ axes represent the plane of space and time. The $V(\phi)$ axis represents the potential energy. And the circle on top of the concave potential is the Higgs particle.

four types of massless bosons: W1, W2, W3, and X. And there are also four types of Higgs particles, which can not be distinguished from each other. After spontaneous symmetry breaking, these four Higgs particles become distinguishable: charged H^+, H^-, and neutral H_0 and h. The W1 boson coupling with the H^+ becomes the massive W^+ boson. And the W2 coupling with the H^- becomes the W^- boson. And the W3 boson combined with the X boson together coupling with the H_0 becomes the Z boson. And the residual component of W3 and X combination becomes the photon.

The h, as one of the four Higgs bosons, is not absorbed by other particles, which is called the Higgs particle in SM. However, there is no constraint on the mass of this Higgs particle in SM.

1.3　The physics beyond the SM

Although the SM explains a lot of facts of current experiments and also achieves another tremendous success on the discovery of the SM-like Higgs boson in 2012. However, the SM cannot explain several important phenomena, and thus it is believed to be an effective theory of a more fundamental theory.

Dark matter and dark energy

As shown in Figure 1.10, the universe is expanding. However, the expansion is accelerating, instead of slowing down. There must be some mysterious force overcomes the attractive force of gravity ad causes the accelerated expansion with time. This unknown force, is usually referred to as "dark energy". Dark here is the thing invisible to us.

The need for dark matter arises from the astronomy observations that the rotational motion of the stars or galaxies suggests a 5∼10 times larger gravitational force than the one could be provided by the matter of the clusters. The lack of matter in this kind of case indicates the existence of matter that couldn't be observed by us, which is called "dark matter".

The current compositions of matter and energy of our universe, from studies, are about 4.9% normal matter (like stars, planets, etc.), 26.8% dark matter, and 68.3% dark energy. The neutrinos of the SM, are stable and have tiny masses, and also interact weakly with other particles. So on a cosmic scale, they behave like the dark matter. However, the redundancy of dark matter (26.8%) over normal matter (4.9%)

suggests that neutrinos are insufficient to explain the observed amount of dark matter.
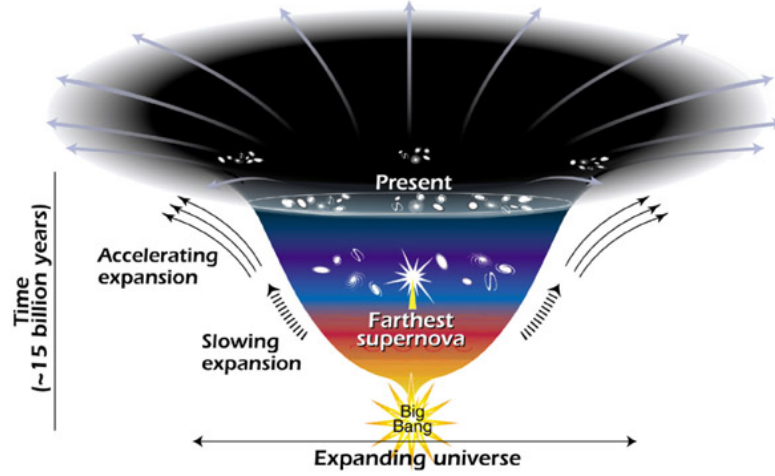
This diagram reveals changes in the rate of expansion since the universe's birth 15 billion years ago. The more shallow the curve, the faster the rate of expansion. The curve changes noticeably about 7.5 billion years ago, when objects in the universe began flying apart at a faster rate. Astronomers theorize that the faster expansion rate is due to a mysterious, dark force that is pushing galaxies apart.

Figure 1.10: Accelerating expansion of the universe [8].

The hierarchy problem

As shown in Table 1.1, the gravitational force is quite small compared to other three forces. It is about 10^{-30} smaller than the weak force. This large discrepancy of scale is called the hierarchy problem of the SM.

The more formal way to state the hierarchy problem is why the Higgs mass in SM is in the scale of $\approx$125 GeV, rather not 10^{18} GeV, while the latter is more natural [9].

Baryon-anitbaryon asymmetry

The imbalance in baryonic matter and anti-baryonic matter in our observed universe can not be explained by the SM, while the Big Bang should produce equal

amount of matter and antimatter.

Gravitation

The graviton is the mediator for gravitational force in SM. However, it has not been found yet. Unlike the QED and QCD, there is no known way to explain relativity in SM.

Since SM leaves us a lot of mysteries, the scientific research towards a better understanding of our universe has never been stopped. The LHC, the largest hadron collider of the world, by colliding energetic protons, simulates the early age of the universe after the Big Bang. In this thesis, two searches for physics beyond the SM are conducted with the CMS detector at LHC.

Chapter 2

The CMS detector at the LHC

The LHC overview

The Large Hadron Collider (LHC), as shown in Figure 2.1, is the world′s largest and most powerful particle accelerator. It is a big underground ring of ≈2.7 km in circumference, sitting on the border of France and Switzerland. Inside the ring, the two high-energy proton beams are guided by the magnetic force, and then collide head-to-head in the positions of the four detectors: CMS, ATLAS, LHCb, ALICE.

At LHC, each proton beam has ≈2000 bunches and each bunch has 10^{11} protons. There is one bunch crossing (collisions of bunches) every 25 ns. The large collision energy, the enormous amount of collisions and especially the large rate of bunch crossing raise a big challenge for detecting the events after the collisions.

The focus of this chapter is to present a brief overview of the Compact Muon Solenoid (CMS) detector. Before that, the coordinate system of CMS is first intro-
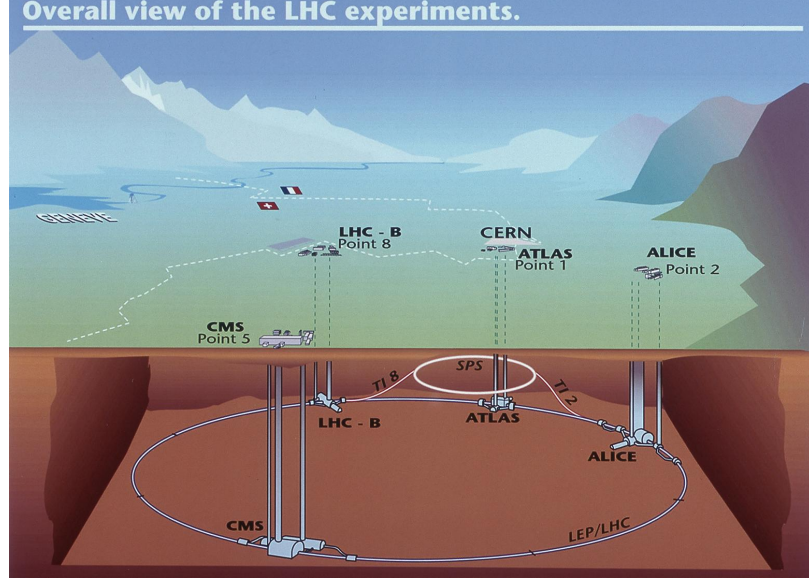
Figure 2.1: An overview of the LHC [10].

duced.

The coordinate system of CMS

In CMS, the z-axis is the along the beam line. The y-axis is vertically upward and the x-axis is directed radially inward the center of the LHC ring. As shown in Figure 2.2, the beam line, which is the z-axis, is perpendicular into this paper. And the x- and y-axes are on this paper but perpendicular to each other.

The default CMS x-y-z coordinate system and also the r-θ-ϕ coordinate system are both right-handed. In the transverse plane (x-y plane), which is shown in Figure 2.2, the azimuthal angle ϕ is defined as the angle measured from the x-axis ($\tan\phi = y/x$). And the transverse momentum p_T is defined as $p_T = \sqrt{p_x^2 + p_y^2}$. The polar angle θ is defined with respect to the the positive z-axis ($\tan\theta = \sqrt{x^2 + y^2}/z$).
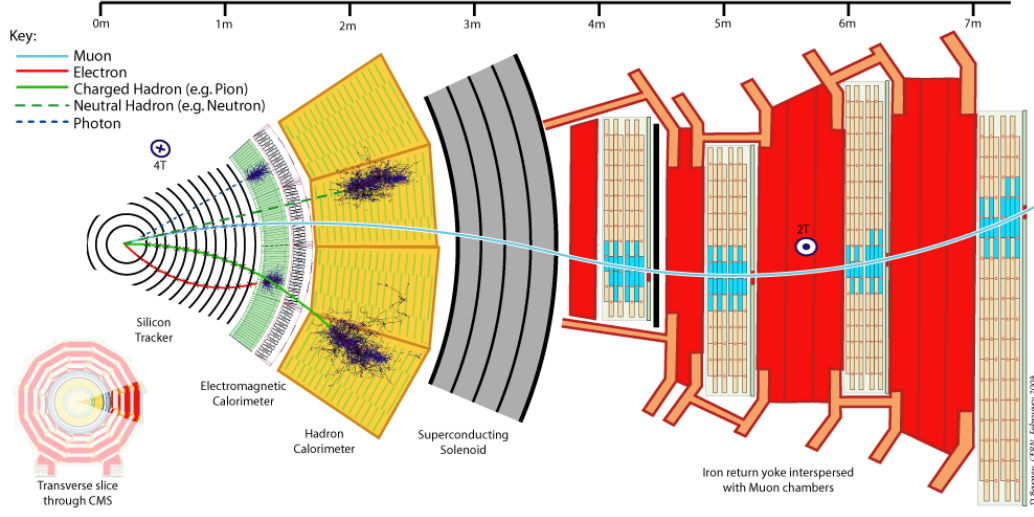
Figure 2.2: Transverse picture of the CMS detector.

The pseudorapidity η, as shown in Figure 2.3 is defined as $\eta = -\ln \tan\left[\frac{\theta}{2}\right]$. And the rapidity is defined as $y = \frac{1}{2}\ln\frac{E+p_z c}{E-p_z c}$.

The CMS detector overview

Along the beam line of LHC, there are four detectors: CMS, ATLAS, LHCb, ALICE. CMS is short for Compact Muon Solenoid, which indicates its profession in muon detecting. The overall layout of CMS from different view points are shown in Figure 2.2 and Figure 2.4. In Figure 2.2, the z axis is perpendicular into this paper. In Figure 2.4, the z axis is on this paper, though the center of the detector.

The dimensions of the CMS detectors are a length of 21.6 m, a diameter of 14.6 m and a total weight of 12500 tons. From the beam line to the outside exterior, which is exactly from the left hand to the right hand of Figure 2.2, there are silicon tracker, Electromagnetic Calorimeter, Hadronic Calorimeter, SuperConducting
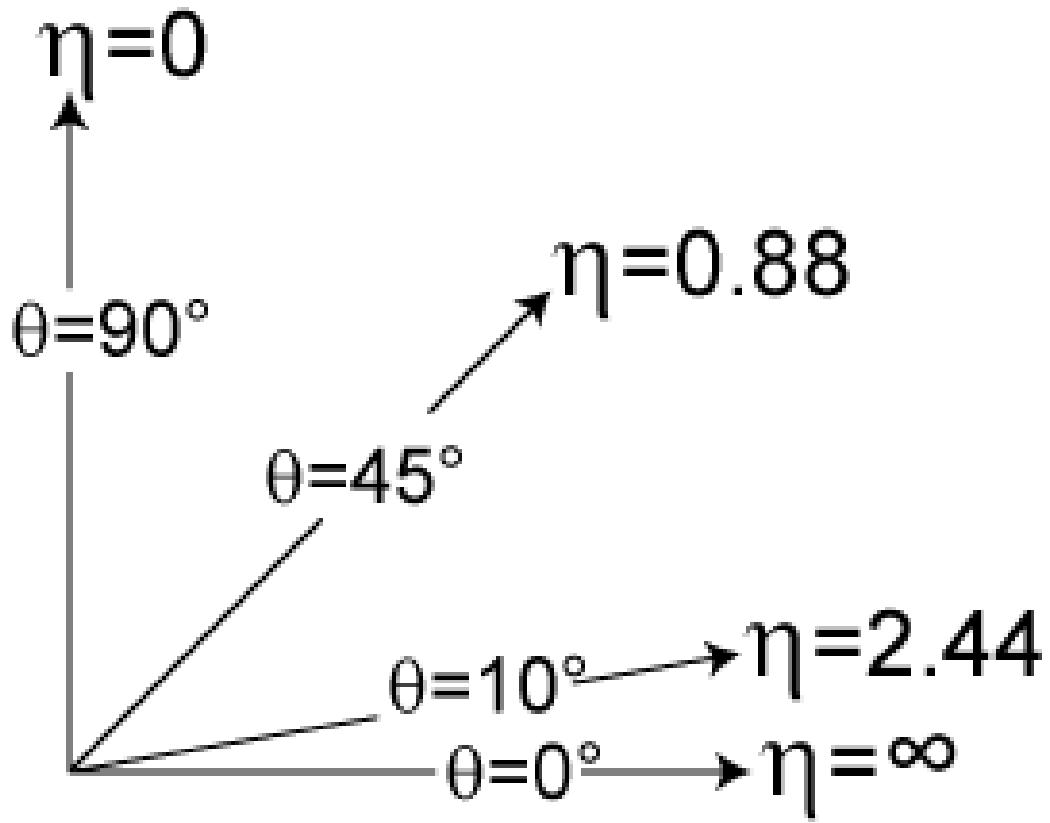
Figure 2.3: The pseudorapidity η and the θ [11].
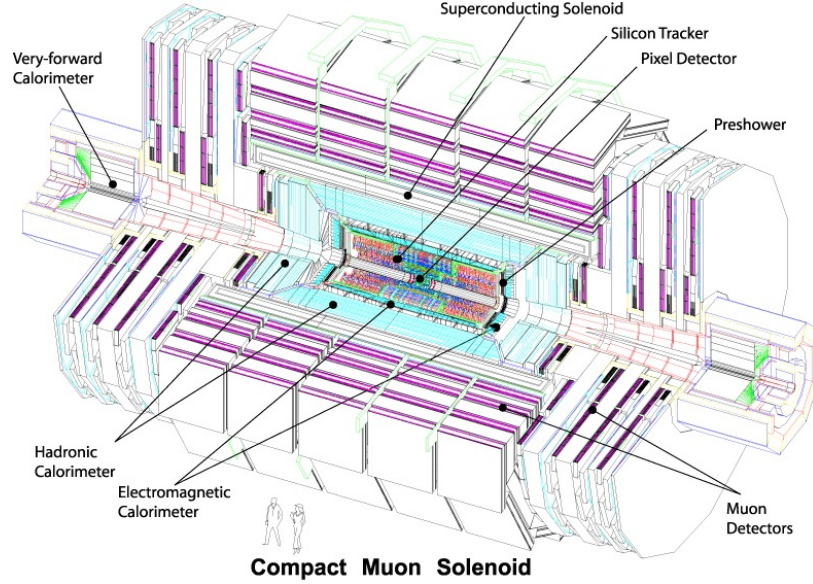
Solenoid, Muon stations.

Figure 2.4: An exploded view of the CMS detector.

2.1   The Magnet

Each beam of LHC has 4 TeV energy in 2013, and it will reach 6.5 TeV in 2015, and 7 TeV in 2016. Particles from such energetic collisions are likely to have high p_T. So in CMS, to achieve a larger bending power of the high-p_T charged particles, thus to get a better momentum resolution, a large magnetic field of 4 T is chosen. In classical Electromagnetism, for a current of 1 Ampere in a loop of radius 3 m, the resulting magnetic field is $\approx 10^{-7}$ T. So in CMS, to generate a field of 4 T for a radius of ≈ 3 m, as shown in Figure 2.2, a super large current 19.5 kA is applied, with 2168

turns of coil. CMS solenoid uses a high-purity aluminium-stabilised conductor and indirect cooling by thermosyphon to achieve superconducting.

The radius of the CMS solenoid is chosen to be large enough to accommodate the inner tracker and the calorimetry inside. The detailed parameters of this are shown in Table 2.1.

Table 2.1: Parameters of the CMS superconducting solenoid.

Characteristics	Values
Field	4 T
Inner Bore	5.9 m
Length	12.9 m
Number of turns	2168
Current	19.5 kA
Store energy	2.7 GJ
Hoop stress	64 atm

2.2 The inner tracking system

As shown in Figure 2.2, the particles resulting from the collision point first pass through the silicon tracking detector. As we mentioned earlier, the enormous amount of collisions will produce a huge particle flux. For the tracker system, beside the

challenge of radiation damage, the responsive time should be very fast and also the space resolution should be very accurate. These two aspects are the main design targets of the silicon tracker system. Here the overview and also details of the silicon tracker system are presented.

The overall tracking volume is given by a cylinder of length of 5.8 m and diameter of 2.6 m. It is mainly composed of two parts: the inner pixel tracker and the layers of the outer strip tracker.

Three layers of silicon pixel detectors are placed closed to the interaction region to improve the measurement of impact parameter [1] of charged-particle tracks, as well as the position of secondary vertices. In addition, CMS uses 10 layers of silicon microstrip detector, which provide the required granularity and precision. The detailed layout of the tracker system is shown in Figure 2.5.
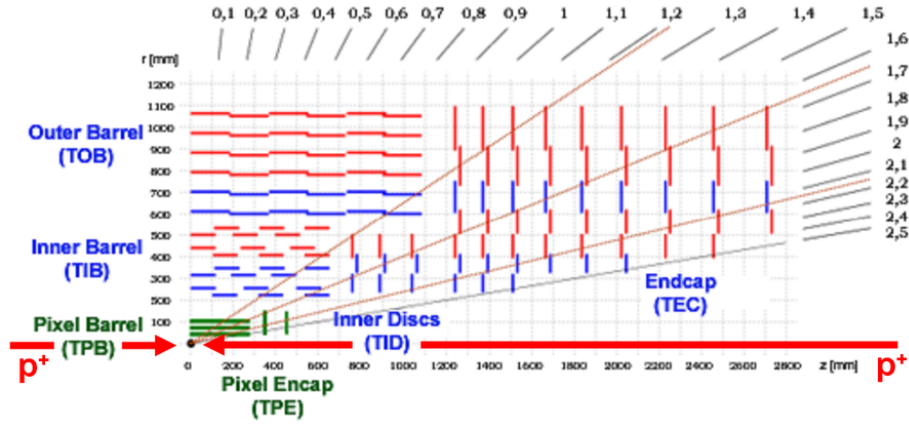

Figure 2.5: The tracker layout of CMS.

---

[1]The details about what impact parameter is could be found : http://en.wikibooks.org/wiki/LaTeX/Footnotes_and_Margin_Notes

The pixel detector

Close to the interaction vertex, in the barrel region, are 3 layers of hybrid pixel detectors at a radii of 4.4, 7.3, and 10.2 cm, which is about the size of a shoe box, as shown in Figure 2.6. Each layer is spilt into sensor segments like mosaic tiles. Each silicon sensor, with the size of 100×150 $(\mu m)^2$, is about two hairs' widths. The endcap of pixel detector is composed of two disks of pixel modules on each side of the barrel region, extending from 6 to 15 cm in radius.
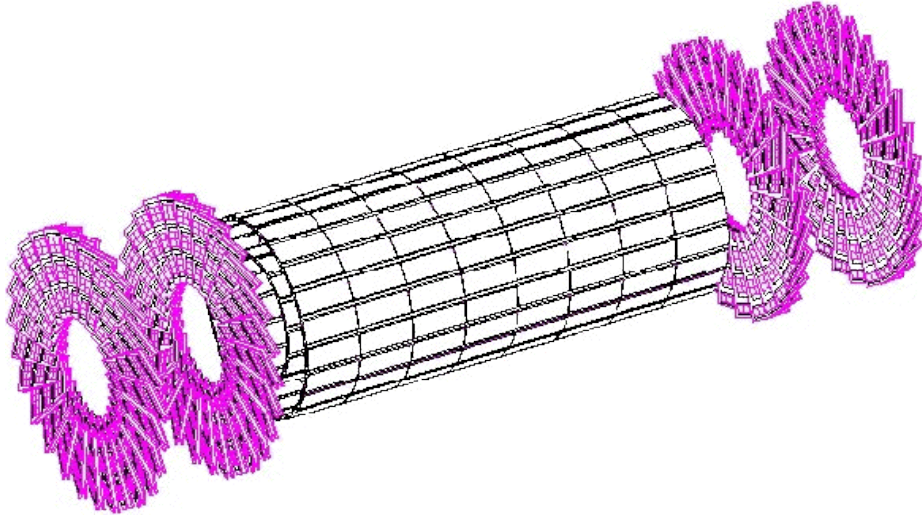

Figure 2.6: Layout of the pixel detector in the CMS [12].

When a charge particle passes trough the sensor, it raises an electronic signal. Knowing which pixels have been passed allows us to reconstruct the charged particle's trajectory. Because the pixel detector is made of 2D tiles, and has three layers, a three-dimensional picture of the particle's motion is created. The spatial resolution of the pixel detector is ≈ 10 μm for the $r-\phi$ measurement and ≈ 20 μm for the z

measurement.

The strip detector

After passing through the three pixel layers, particles travel through ten layers of silicon strip detectors, as shown in Figure 2.7, which reaches out to a radius of 130 cm. The silicon strip tracking detector consists of four inner barrel (TIB) layers assembled in shells with two inner endcaps (TID), each composed of three small discs. The outer barrel (TOB) consists of six concentric layers. Finally two endcaps (TEC) close off the tracker. Each part of the strip detector has silicon modules designed differently for its place within the detector.

Unlike the 2D pixel sensor, most of the 10 strip layers are composed of 1D strip sensors. So when a charged particle passes through the strip sensor, the strip detector only outputs the local 1D position instead of 2D position.

2.3   Electromagnetic calorimeter (ECAL)

The ECAL is designed to calibrate the energy of electron and photons resulting from proton-proton (pp) collisions at LHC, and its structure is shown in Figure 2.8. ECAL uses lead tungstate ($PbWO_4$) crystals with coverage in $|\eta|$ up to 3.0. The lead tungstate crystal is highly transparent and "scintillates" when electrons and photons pass through it, which produces light in proportion to the charged particles′ energy. It also has short radiation (0.89 cm) and Moliere (2.2 cm) lengths, and is fast and
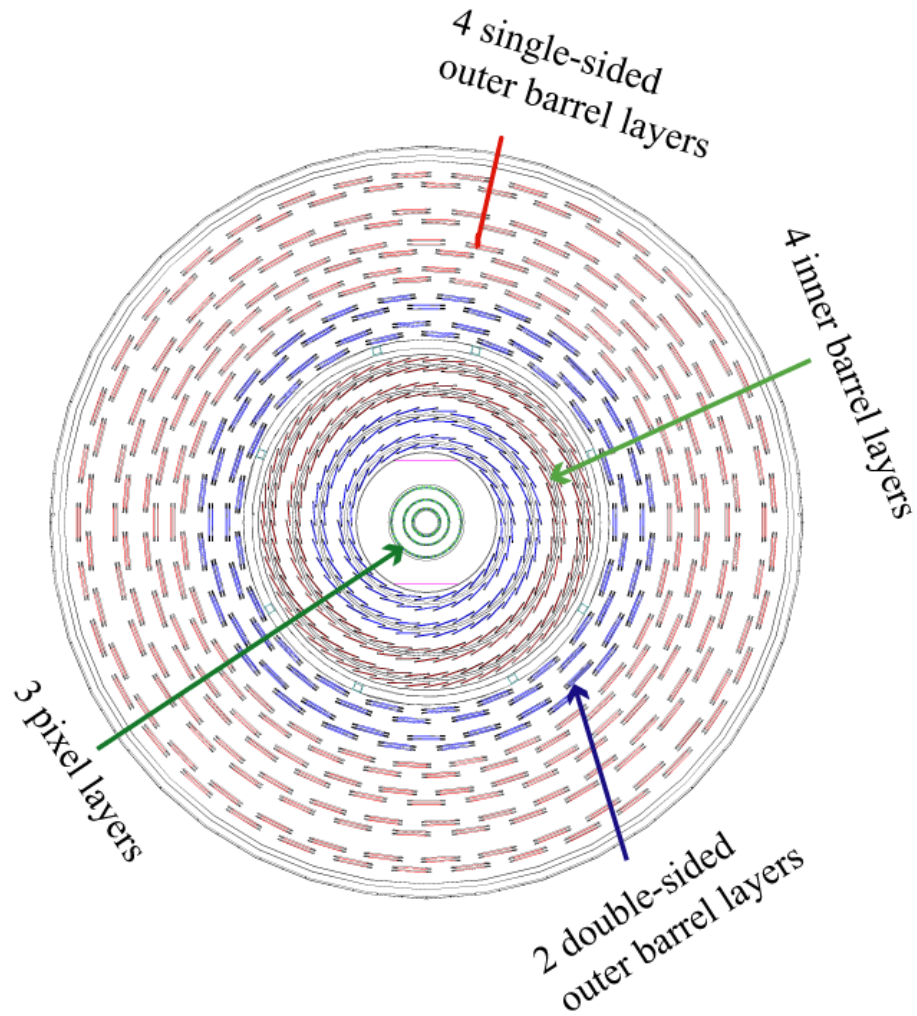
Figure 2.7: Layout of tracker system of CMS, with z-axis perpendicular into the paper.

radiation hard. However, the $PbWO_4$ crystal produces relatively low light yield. So the silicon avalanche photodiodes (APDs), which could amplify the light signal into electric signal, are used as photodetectors in the ECAL barrel (EB) and vacuum phototriodes (VPTs) in the ECAL endcap (EE).
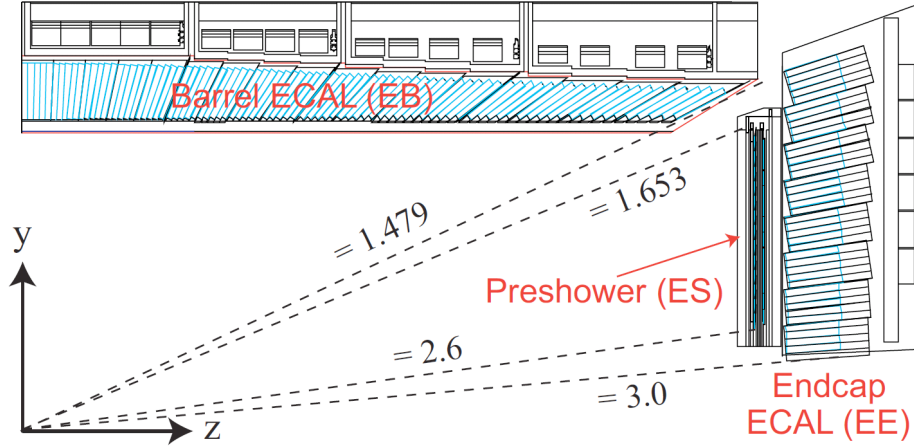

Figure 2.8: Geometric view of one quarter of the ECAL.

These photodetectors have been especially designed to work within the high magnetic field. They are glued onto the back of each of the crystals to detect the scintillation light and convert it to an electrical signal that is amplified and sent for analysis.

A preshower system is installed in front of the EE. The preshower is made of two planes of lead followed by silicon sensors. The reason for the preshower system is that short-lived particles called neutral pions, produced in pp collisions, can inadvertently mimic high-energy photons when they decay into two closely-spaced lower energy photons that the ECAL picks up together. And for Higgs discovery, the high energy

photons from Higgs decay is the important signature of $H \to \gamma\gamma$ channel. So the preshower system could identify the photons from neutral pion decay and distinguish them from the photons of $H \to \gamma\gamma$ decay.

2.4 Hadronic calorimeter (HCAL)

HCAL is designed to measure the energy of hadrons and also the transverse missing energy E_T^{miss}. Improving the energy resolution and achieving good hermeticity for the the E_T^{miss} measurement, are the two main goals of HCAL design.

As shown in Figure 2.9, HCAL is composed by four parts, HCAL barrel (HB), HCAL endcap (HE), HCAL outer (HO) and HCAL forward (HF). HF, not presented in the plot, sits on the outside of the muon stations and covers $3 < |\eta| < 5.0$.

Brass is the filling material of HCAL. It is chosen because it is non-magnetic and has short interaction length. To achieve a good containment, HCAL maximizes the brass inside of the solenoid by minimizing the detection material with the application of the tile/filbre technology [12]. HCAL is a sample detector, in which layers of brass are interleaved by layers of fibre. The HO is located outside of the solenoid, to complement the measurement of HB.
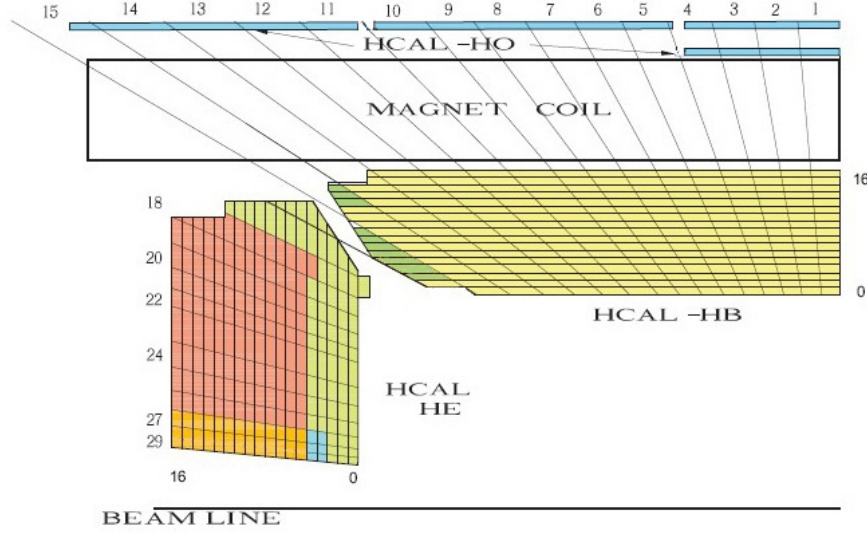
Figure 2.9: Geometric view of one quarter of the HCAL.

2.5 Muon system

The layout of one quarter of the CMS muon system for the initial low luminosity running is shown in Figure 2.10, and the transverse view of the muon stations (MSs) is shown in Figure 2.11, with z-axis perpendicular into the paper. In Figure 2.11, the red colored part is the return yoke, which has a magnetic field of 2 T. As shown in Figures 2.10 and 2.11, in the Muon Barrel (MB) region, 4 stations of detectors are arranged in cylinders interleaved with the iron yoke. This magnetic field in the return yoke bends the trajectory of muon, while there is almost no magnetic field in the four muons stations (MS1, MS2, MS3, MS4). In the adjacent muon stations by comparing the bending angle because of the return yoke , the muon system correctly calculates the muon momentum.
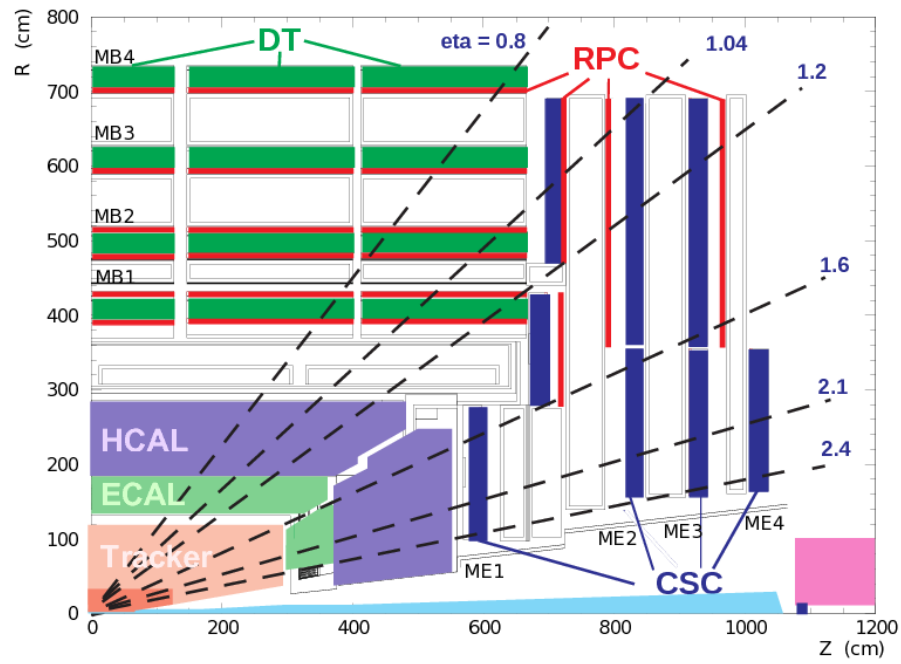
Figure 2.10: Layout of one quarter of the CMS muon system for initial low luminosity running. The RPC system is limited to $|\eta| < 1.6$ in the endcap, and for the CSC system only the inner ring of the ME4 chambers have been deployed.
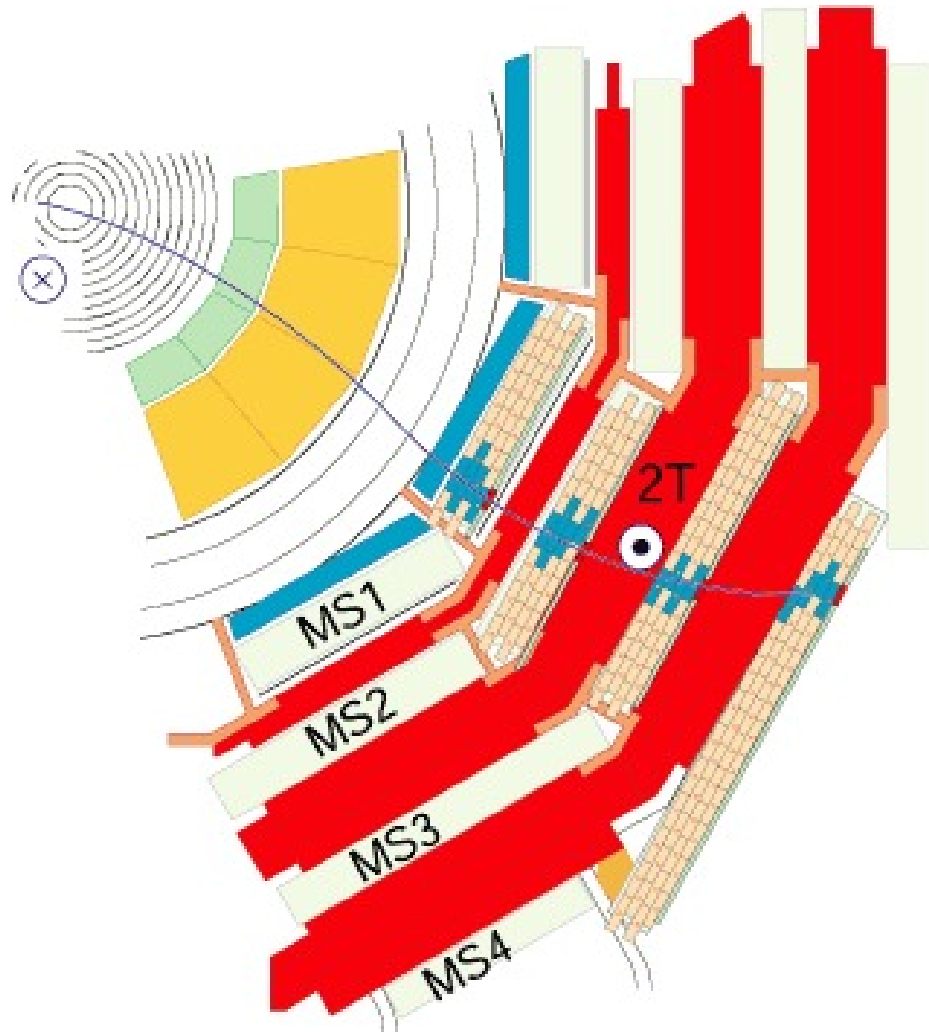
Figure 2.11: The Muon stations in the transverse view.

From Figure 2.10, three types of gaseous detectors are used to identify and measure muons: drift tube (DT), cathode strip chamber (CSC), and resistive plate chamber (RPC).

Drift tube (DT), with detailed layout in Figure 2.12, is used in the barrel region ($|\eta| < 1.2$). In this region, the residual magnetic field in the chambers is low and also muon rate is low, so drift tube is chosen. When a muon or any charged particle passes through the gas volume, it knocks electrons off the atoms of the gas. These electrons follow the electric field ending up at the positively-charged wire (anode wire in Figure 2.12). By registering where in the wire and also the time the electrons take to reach the wire, the DT could provide a 2D position of the passing charged particle. The maximum drift length is 2.0 cm and the single point resolution is $\approx 200 \ \mu m$.

In the endcap region, cathode strip chambers (CSCs) are used because of the high residual magnetic field and also high muon rate. As shown in Figure 2.13, CSCs consist of arrays of positively-charged "anode" wires crossed with negatively-charged copper "cathode" strips within a gas volume. When muons pass through, they knock electrons off the gas atoms, which flock to the anode wires producing an avalanche of electrons. Positive ions move away from the wire and towards the copper cathode, also inducing a charge pulse in the strips, at the right angles to the wire direction. Because the strips and the wires are perpendicular, we get two position coordinates for each passing charged particle.

In addition to this, resistive plate chambers (RPCs), as shown in Figure 2.14,
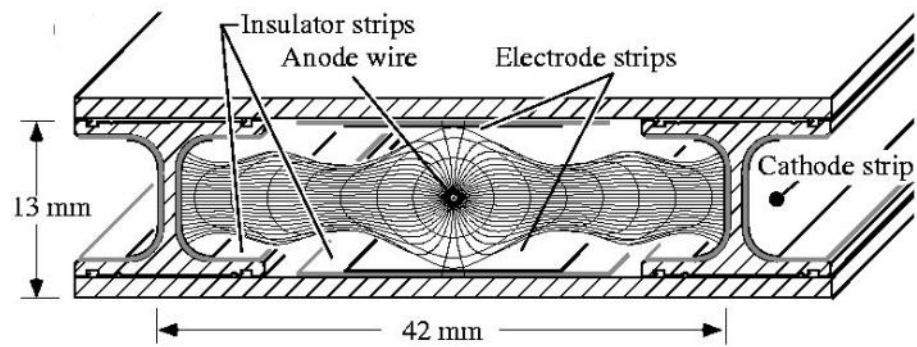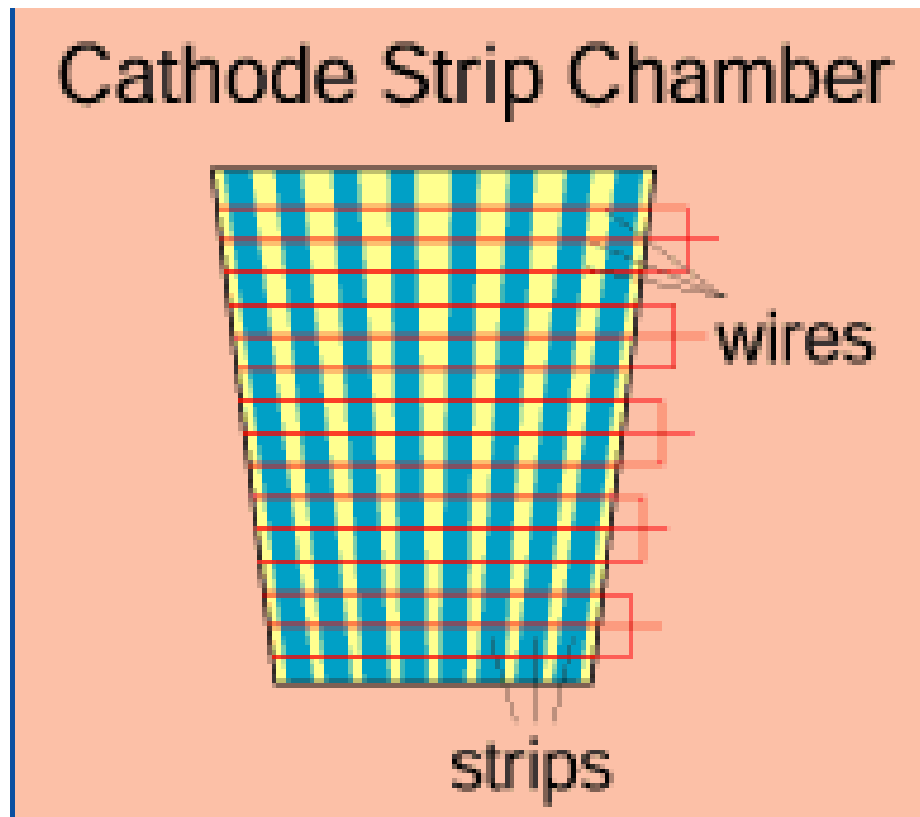
Figure 2.12: Layout of the drift tube [13].

Figure 2.13: Layout of the drift tube [14].

are used in both the barrel and the endcap regions. The RPCs could provide a fast response with a good time resolution but with a coarser position resolution than the DTs and the CSCs. So the RPCs could identify the correct bunch crossing (25 ns per bunch crossing).
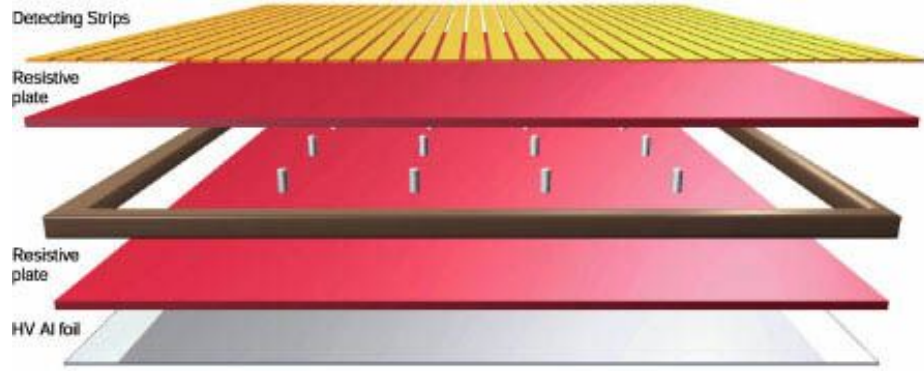

Figure 2.14: Layout of the resistive plate chamber [14].

Muons from pp collisions are measured 3 times: in the silicon tracking system, after the solenoid coil, and in the muon chambers (the muon system). Measurement of the momentum of muons using only the muon system, is essentially determined by the muon bending angle when it exits the 4 T solenoid, taking the interaction point of pp collision as the origin of the muon. For low-momentum muons, the best momentum resolution is given by the resolution obtained in the silicon tracker. For high-momentum muons, combining the inner tracker and muon detector measurements will highly improve the muon momentum resolution. At CMS, in $0 < |\eta| < 2.0$, for μ with p_T 200~400 GeV , $\Delta p/p$ is measured to be $\leq 3\%$.

2.6   Trigger and data acqusition

As mentioned earlier, there is one bunch crossing per 25 ns. While for each bunch crossing, there is ≈40 millions pp collisions. Although the readout of CMS is fast enough, it costs a lot to store this amounts of events. So CMS adopts a two-level trigger system to filter out the uninteresting events.

The Level-1 (L1) trigger is automatic and universally applied to each event, with the application of hardware processors. Basically, L1 trigger sets a threshold for "trigger primitive" objects, like photon, muon, electron, and jets to be above some E_T or p_T. After the L1 trigger, the event rate reduces to 100 kHz.

The L2 trigger, which is also named as high level trigger (HLT), is used to further reduce the 100 kHz to 100 Hz event rate. In L2 trigger system, the event from pp collision is partially reconstructed. Information about the calorimeter and muons is first reconstructed and compared with the threshold of L2. Events falling this threshold will be immediately thrown out. Then information of pixel tracks is reconstructed and tested with the corresponding threshold. Following this kind of process, without reconstructing all possible objects in an event, L2 is more flexible and has complete freedom in selecting events.

Data, after the trigger system, is fully reconstructed, and taped on the disks.

Chapter 3

Search for $X \rightarrow qV$ or VV at LHC at $\sqrt{s} = 8$ TeV

3.1 Introduction

As we mentioned in Chapter 1, the SM is limited and couldn't provide solutions for some important phenomena, for example, the existence of graviton, the three generations of quarks and leptons, etc. Several models of physics beyond the standard model (SM) predict the existence of resonances with masses above 1 TeV that decay into a quark and a W or Z vector boson, or into two vector bosons. In proton-proton (pp) collisions at the energies reached at the Large Hadron Collider (LHC), vector bosons emerging from such decays usually would have sufficiently large momenta so that the hadronization products of their $q\bar{q}'$ decays would merge into a single massive

jet [15]. We present a search for events containing one or two jets of this kind in pp collisions at a centre-of-mass energy of $\sqrt{s} = 8$TeV. The data sample, corresponding to an integrated luminosity of 19.7 fb^{-1}, was collected with the CMS detector at the LHC.

The signal is characterized by a peak in the dijet invariant mass distribution m_{jj} over a continuous background from SM processes, comprised mainly of multijet events from quantum chromodynamic (QCD) processes. The sensitivity to jets from W or Z bosons is enhanced through the use of jet-substructure techniques that help differentiate such jets from remnants of quarks and gluons [16, 17], providing the possibility of "W/Z-tagging". This search is an update of a previous CMS study [18] performed using data from pp collisions at $\sqrt{s} = 7$ TeV. Besides increased data-sample size and larger signal cross sections from the increase in centre-of-mass energy, this analysis also benefits from an improved W/Z-tagger based on "N-subjettiness" variables, introduced in Ref. [19] and defined in Section 3.2.

We consider four reference processes that yield one W/Z-tagged or two W/Z-tagged all-jet events: (i) an excited quark $q*$ [20, 21] that decays into a quark and either a W or a Z boson, (ii) a Randall–Sundrum (RS) graviton G_{RS}that decays into WW or ZZ bosons [22, 23], (iii) a "bulk" graviton G_{Bulk} that decays into WW or ZZ [24–26], and (iv) a heavy partner of the SM W boson (W') that decays into WZ [27].

Results from previous searches for these signal models include limits placed on the production of $q*$ at the LHC as dijet [28–30] or γ+jet [?] resonances, with a $q*$ lighter

than $\approx$3.5TeVat a confidence level (CL) of 95% [28]. Specific searches for resonant

qW and qZ final states at the Tevatron [31,32] exclude $q*$ decays into qW or qZ with

$m_{q*} < 0.54TeV$, and results from the LHC [18,33] exclude $q*$ decays into qW or qZ

for $m_{q*} < 2.4TeV$ and $m_{q*} < 2.2TeV$, respectively.

Resonances in final states containing candidates for WW or ZZ systems have also

been sought [34–37], with lower limits set on the masses of $G_{\mathrm{RS}}$and G_{Bulk}as a func-

tion of the coupling parameter $k/\overline{M}_{\mathrm{Pl}}$, where k reflects the curvature of the warped

space, and $\overline{M}_{\mathrm{Pl}}$ is the reduced Planck mass ($\overline{M}_{\mathrm{Pl}} \equiv M_{\mathrm{Pl}}/\sqrt{8\pi}$) [22, 23]. The bulk

graviton model is an extension of the original RS model that addresses the flavour

structure of the SM through localization of fermions in the warped extra dimension.

The experimental signatures of the $G_{\mathrm{RS}}$and G_{Bulk} models differ in that G_{Bulk} favours

the production of gravitons through gluon fusion, with a subsequent decay into vector

bosons, rather than production and decay through fermions or photons, as the cou-

pling to these is highly suppressed. As a consequence, G_{Bulk} preferentially produces

W and Z bosons that are longitudinally polarized, while G_{RS}favours the production of

transversely polarized W or Z bosons. In this study, we use an improved calculation

of the G_{Bulk} production cross section [24] that predicts a factor of four smaller yield

than assumed in previous studies [34, 35].

The most stringent limits on W'boson production are those reported for searches

in leptonic final states [38, 39], with the current limit specified by $m_{W'} > 2.9TeV$.

Depending on the chirality of the W' couplings, this limit could change by $\approx$0.1TeV.

Searches for W' in the WZ channel have also been reported [**?**, 35, 40] and set a lower

limit of $m_{W'} > 1.1 TeV$.

The CMS detector, the data, and the event simulations are described briefly in

Section **??**. Event reconstruction, including details of W/Z-tagging, and selection cri-

teria are discussed in Section 3.2. Section 3.9.1 presents studies of dijet mass spectra,

including SM background estimates. The systematic uncertainties are discussed in

Section 3.9, the interpretation of the results in terms of the benchmark signal models

is presented in Section 3.11, and the results are summarized in Section 3.12.

3.2 Dijet analysis with jet substructure tagging

3.3 Event display

The event detected by the CMS detector is shown in Figure 3.1 and Figure 3.2. In Figure 3.1, the top image is showing the event in the transverse plane, which is global $\theta - \phi$ axes. The bottom image is showing this event in the $\theta - z$ plane. In Figure 3.2, the top image is showing the global view of this event. And the bottom image is showing the lego plot of the two jets, each of which is composed by two subjets, a term that we will introduce in the following text.

3.3.1 Jet reconstruction

Based on CMSSW 5.3.x software package,events are reconstructed using the particle-flow reconstruction algorithm [41], which attempts to reconstruct all stable particles in an event by combining information from all subdetectors. The algorithm categorizes all particles into five types: muons, electrons, photons, charged and neutral hadrons. The resulting particle flow candidates are passed to each jet clustering algorithm, in this case the Cambridge-Aachen (CA) [42, 43] jet clustering algorithm, as implemented in FastJet version 3.0.1 [44, 45], to create "particle flow jets". The

CMS Experiment at LHC, CERN
Data recorded: Sun Oct 7 17:44:20 2012 EDT
Run/Event: 204601 / 869076077
Lumi section: 752
invariant mass = 2163.7

et = 487.40
eta = 0.145
phi = 0.202
mass = 10.63

et = 291.95
eta = 0.446
phi = -3.120
mass = 11.14

et = 350.55
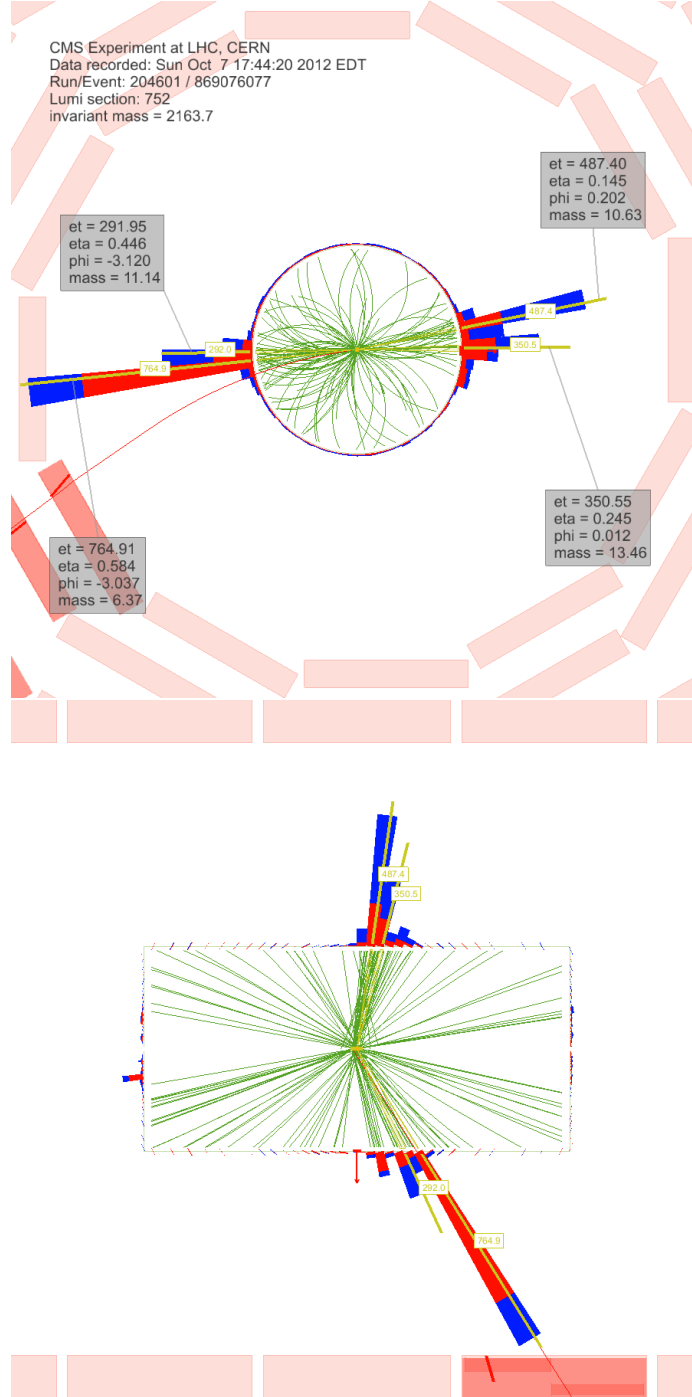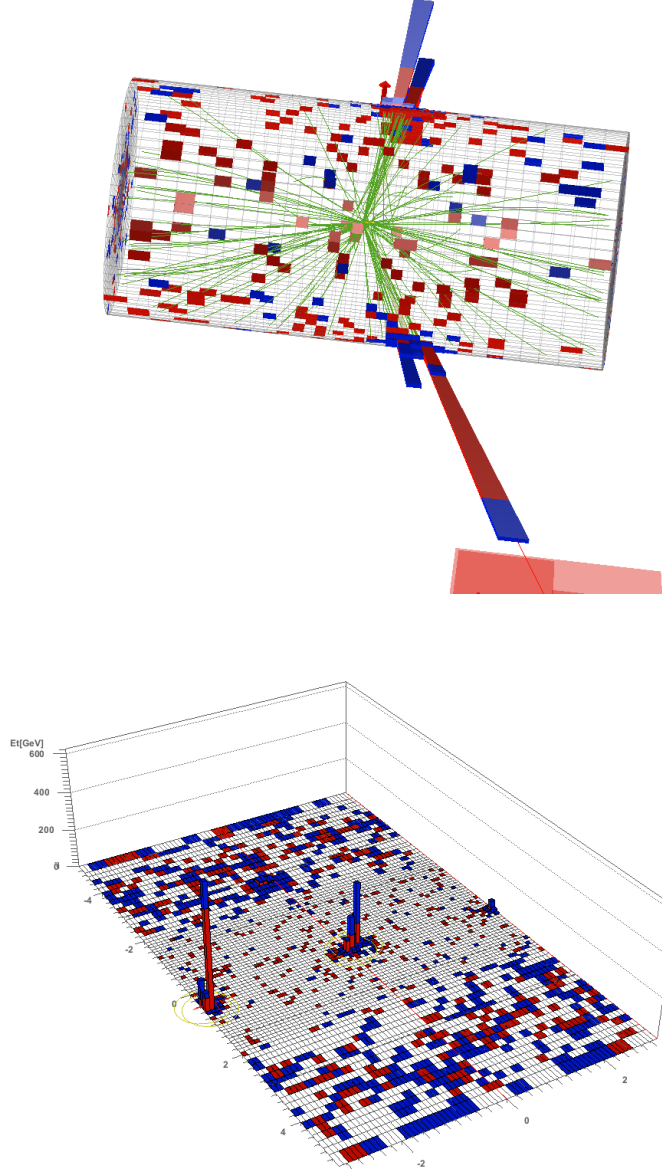eta = 0.245
phi = 0.012
mass = 13.46

et = 764.91
eta = 0.584
phi = -3.037
mass = 6.37

Figure 3.1: Event display of double W/Z-tagged event with the highest dijet invariant mass of 2.16 TeV. The transverse momenta of the two leading jets are 1.1 TeVand 0.92 TeV. The invariant mass of the two leading pruned CA8 jets is 97.82 GeVand 85.08 GeV.

Figure 3.2: Event display of double W/Z-tagged event with the highest dijet invariant mass of 2.16 TeV. The transverse momenta of the two leading jets are 1.1 TeVand 0.92 TeV. The invariant mass of the two leading pruned CA8 jets is 97.82 GeVand 85.08 GeV.

CA clustering sequence is only determined by the distance between clusters and is not weighted by their momentum, as is done for the k_{T} and anti-k_{T} algorithms. A distance parameter of size $R = \sqrt{(\Delta \eta)^2 + (\Delta \phi)^2} = 0.8$ is used for the CA algorithm.

Charged hadrons identified as pileup are removed from the inputs to the jet clustering algorithms. The remaining neutral component of pileup is removed by applying a residual area-based correction as described in Ref. [46,47]. The mean p_{T} per unit area is computed with the k_{T} algorithm with the "active area" method, with a distance parameter of 0.6, and the jet energy is corrected by the amount of pileup expected in the jet area. The amount of energy expected from the underlying event is added back into the jet. The pileup-subtracted jet four momenta are finally corrected for nonlinearities in η and p_{T} with simulated data, with a residual η-dependent correction added to correct for the difference in simulated and true responses [48,49].

The jet energy corrections for the CA $R = 0.8$ jets are derived from studies using the anti-k_{T} $R = 0.7$ jet algorithm. Simulation studies confirm that these anti-k_{T}-derived jet corrections are adequate for the CA $R = 0.8$ jet algorithm for the jet momenta considered here [16].

3.3.2 Event selection

Events are selected using the following cuts:

- The event must have a well reconstructed primary vertex as computed by a deterministic annealing filter (DAF) ($|z_{\mathrm{Primary\ Vertex}}| < 24$ cm, $N_{\mathrm{DOF}} > 6$).

- The following recommended noise event filters are used:

  - CSC tight beam halo filter

  - HBHE noise filter with isolated noise rejection

  - HCAL laser event filter (HBHE) and HCAL laser event filter 2012

  - ECAL dead cell trigger primitive (TP) filter

  - The beam scraping filter

  - Bad EE supercrystal filter

  - The tracking failure filter

  - Good primary vertex filter

  - Tracking coherent noise filter

  - Tracking TOBTEC fakes filter

- The events are required to have at least two ungroomed CA8 jets with

  - $p_T > 30$ GeV, $|\eta| < 2.5$

  - to have muon energy fraction < 0.8

  - pass tight particle flow jet ID. The tight PF jet ID is listed below:

    * Neutral Hadron (EM) Fraction $< 0.90 (< 0.90)$, for all jet η

    * Number of Constituents > 1, for all jet η

    * Charged Hadron (EM) Fraction $> 0 (< 0.99)$, for jet $|\eta| < 2.4$

  * Charged Multiplicity> 0, for jet $|\eta| < 2.4$

- Beam background events are removed using the following requirements:

  - In events with at least 10 tracks, a minimum of 25% of these tracks must be high purity tracks.

- We also require $E_T^{miss}/\sum E_T < 0.5$ to further suppress the noise producing large fake E_T^{miss}.

- The events must pass $|\Delta\eta| < 1.3$, $m_{jj} > 890 GeV$

This sample of dijet events is then tested for presence of hadronically decaying W or Z bosons.

3.4   Data and Monte Carlo samples

The data sample of proton-proton collisions at $\sqrt{s} = 8$ TeVwas collected in 2012 and corresponds to an integrated luminosity of 19.7 fb^{-1}. The datasets and also the certifications used are summarized in Table 3.1. The dijet sample is dominated by light flavored and gluon jets, which we denote as the "QCD background". The QCD background is obtained from data by fitting an analytic parameterization of the dijet invariant mass distribution.

Signal events have been simulated using JHUGEN [50,51], PYTHIA 6.426 [52] and HERWIG++ 2.5.0 [53] event generators and processed through a simulation of the CMS detector, based on GEANT4 [54]. PYTHIA 6 is used with CTEQ61L [55] and HERWIG++ with MRST2001 [56] parton distribution functions. Tune Z2* (a modification of tune Z1 [57]) is used with PYTHIA 6, while the tune version 23 is used with HERWIG++. The process $q^* \to W/Z +$ jet is generated using PYTHIA 6. RS graviton production is studied with $k/\overline{M}_{\mathrm{Pl}} = 0.1$, which determines a resonance width of about 1% of the resonance mass which is about a factor five smaller than the experimental resolution for dijets. While HERWIG++ contains a more detailed description of the angular distributions for G_{RS}than PYTHIA 6 for this process [58] and is therefore used to model the G_{RS}resonance shape, the PYTHIA 6 cross section is used to maintain consistency with reference models used in related analyses [34]. Bulk graviton production is studied with $k/\overline{M}_{\mathrm{Pl}} = 0.2$ and is generated with JHUGEN interfaced with PYTHIA 6 for the showering. Bulk graviton cross sections are cal-

culated using CalcHEP. The process $W' \to WZ$ is generated using PYTHIA 6 with Standard Model $V - A$ couplings and without applying k-factors.

To validate our RS graviton resonance Monte Carlo, we compare Pythia6, Herwig++ and a generator including full angular correlations developed by the JHU group (which we denote "JHU generator"). Figure 3.3 shows the comparsions of invariant mass and $\Delta\eta$ of two Z bosons at generator level, in which Herwig++ and Pythia6 are compared with the JHU generator which describes the angular distributions exactly. Pythia6 does not implement the angular correlations, and from Figure 3.3 one can indeed conclude that in its description of this effect it is inferior to Herwig++.
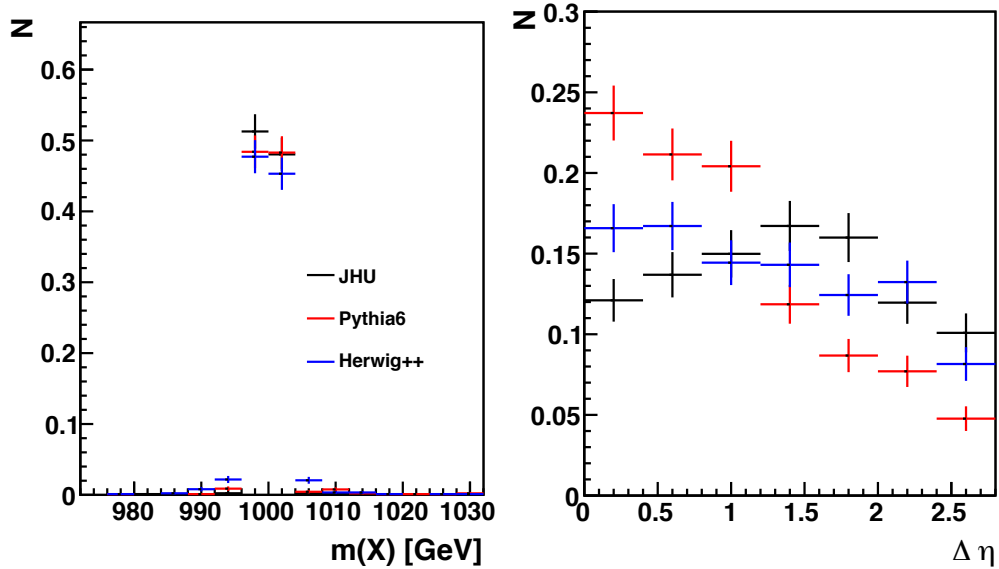
Figure 3.3: Invariant mass and $\Delta\eta$ of two Z bosons at generator level for Pythia6 and Herwig++ models of a 1 TeVRS graviton resonance with $k/M_{PL} = 0.02$ with the JHU generator which includes all angular correlations.

All Monte Carlo events are fully simulated and reconstructed via the Geant4-based CMS simulation and reconstruction software.

Tables 3.2, 3.3, 3.5 and 3.4 summarize the new physics simulation datasets used in this analysis.

Dataset
/Jet/Run2012A-22Jan2013-v1/AOD
/JetHT/Run2012B-22Jan2013-v1/AOD
/JetHT/Run2012C-22Jan2013-v1/AOD
/JetHT/Run2012D-22Jan2013-v1/AOD

Table 3.1: Summary of 8 TeVcollision data used in this analysis. The certification file used for these data is `Cert_190456-208686_8TeV_22Jan2013ReReco_Collisions12_JSON.txt` .

Table 3.2 describes a single-tagged process: $q* \to W/Z + jet$ with a large cross section. We generated the MC using Pythia6 with Tune Z2*. The configuration is in the appendix of this note. The parameters `RTCM(43)`, `RTCM(44)`, `RTCM(45)` are set to 1 and the scale `RTCM(41)` is set to the resonance mass `PMAS(343,1)=PMAS(344,1)`. Only decays in to qW or qZ are allowed. We generate the process $q* \to W/Z + jet$ using Pythia6 with Tune Z2*.

Table 3.3 shows a double-tagged process: $G_{RS} \to WW/ZZ$. This is produced using Herwig++ with Tune23 and as a cross check also in Pythia6 with Tune Z2*. In Pythia6, the parameter `PARP(50)` corresponding to $5.4k/\bar{M}_{Pl}$ which impacts the

Process	Generator	Events	X-sec[pb]
qW(m=750GeV)	Pythia6	30000	1.133E+02
qW(m=1000GeV)	Pythia6	30000	2.647E+01
qW(m=1500GeV)	Pythia6	30000	2.540E+00
qW(m=2000GeV)	Pythia6	30000	3.510E-01
qW(m=3000GeV)	Pythia6	30000	1.008E-02
qZ(m=750GeV)	Pythia6	30000	4.071E+01
qZ(m=1000GeV)	Pythia6	30000	9.405E+00
qZ(m=1500GeV)	Pythia6	30000	8.937E-01
qZ(m=2000GeV)	Pythia6	30000	1.231E-01
qZ(m=3000GeV)	Pythia6	30000	3.465E-03

Table 3.2: Summary of the simulated Monte Carlo samples used in this analysis for process $q* \to Z/W + jet$

width and cross section of the resonance. In Herwig++, the cross section and width are given by the ratio of `RS/Model:Lambda_pi` and the resonance mass `/Herwig/Particles/Gravito`. The process $G_{RS} \to WW/ZZ$ is generated using Herwig++ with Tune23 and its cross section is taken from Pythia6 with Tune Z2*. We study RS graviton production with $k/\bar{M}_{Pl} = 0.1$, defining a resonance width smaller than the experimental resolution for dijets. Table 3.4 describes another double-tagged process: $W' \to WZ$. This is produced using Pythia6 with Tune Z2*. The decay of the W' is restricted to WZ with `MDME(331,1)=1`. The process $W' \to WZ$ is generated using Pythia6 with Tune Z2*.

All Monte Carlo events are fully simulated and reconstructed via the CMS simulation

and reconstruction software.

Process	Generator	Events	Pythia6 x-sec [pb]
WW(m=750GeV)	Herwig++/Pythia6 Z2*	30000	2.220E+00
WW(m=1000GeV)	Herwig++/Pythia6 Z2*	30000	4.254E-01
WW(m=1500GeV)	Herwig++/Pythia6 Z2*	30000	3.298E-02
WW(m=2000GeV)	Herwig++/Pythia6 Z2*	30000	4.083E-03
WW(m=2500GeV)	Herwig++/Pythia6 Z2*	30000	6.191E-03
WW(m=3000GeV)	Herwig++/Pythia6 Z2*	30000	1.010E-04
ZZ(m=750GeV)	Herwig++/Pythia6 Z2*	30000	1.120E+00
ZZ(m=1000GeV)	Herwig++/Pythia6 Z2*	30000	2.137E-01
ZZ(m=1500GeV)	Herwig++/Pythia6 Z2*	30000	1.662E-02
ZZ(m=2000GeV)	Herwig++/Pythia6 Z2*	30000	2.027E-03
ZZ(m=2500GeV)	Herwig++/Pythia6 Z2*	30000	3.077E-04
ZZ(m=3000GeV)	Herwig++/Pythia6 Z2*	30000	5.099E-05

Table 3.3: Summary of the simulated Monte Carlo samples used in this analysis for process $G_{RS} \to WW, ZZ$.

Process	Generator	Events	X-sec[pb]
WZ(m=750GeV)	Pythia6	30000	5.391E-01
WZ(m=1000GeV)	Pythia6	30000	1.444E-01
WZ(m=1500GeV)	Pythia6	30000	1.804E-02
WZ(m=2000GeV)	Pythia6	30000	3.129E-03
WZ(m=2500GeV)	Pythia6	30000	6.781E-04
WZ(m=3000GeV)	Pythia6	30000	1.894E-04

Table 3.4: Summary of the simulated Monte Carlo samples used in this analysis for process $W' \to WZ$.

Process	Generator	Events	X-sec[pb]
WW(m=$1000GeV$)	JHU Z2*	50000	0.001774
WW(m=$1500GeV$)	JHU Z2*	50000	9.207E-05
WW(m=$2000GeV$)	JHU Z2*	50000	8.004E-06
WW(m=$2500GeV$)	JHU Z2*	50000	8.851E-07
WW(m=$3000GeV$)	JHU Z2*	50000	-
ZZ(m=$1000GeV$)	JHU Z2*	50000	0.0009044
ZZ(m=$1500GeV$)	JHU Z2*	50000	4.622E-05
ZZ(m=$2000GeV$)	JHU Z2*	50000	4.029E-06
ZZ(m=$2500GeV$)	JHU Z2*	50000	4.460E-07
ZZ(m=$3000GeV$)	JHU Z2*	50000	-

Table 3.5: Summary of the simulated Monte Carlo samples used in this analysis for process $G_{Bulk} \rightarrow WW, ZZ$.

3.5 Trigger

Events are selected if one of the following triggers has fired: HLT_HT750, HLT_PFHT650, HLT_PFNoPUHT650 HLT_FatDiPFJetMass750_DR1p1_Deta1p5. All versions of each of these triggers is used. None of these triggers are prescaled druing the 2012 data taking period. HLT_PFNoPUHT650 trigger is used for the data set after the RunC(including RunC), while HLT_PFHT650 trigger is only used for RunA and RunB data sets.

Figure 3.4, Figure 3.5 and Figure 3.6 shows the trigger efficiencies of the OR of the highest threshold HLT_PFHT650 trigger and the HLT_FatJetMass trigger w.r.t. an OR of the lower threshold HLT_HT550 trigger. From the plot, the trigger is 99% effiecient above $890 GeV$ for the untagged, single tagged and double tagged data.
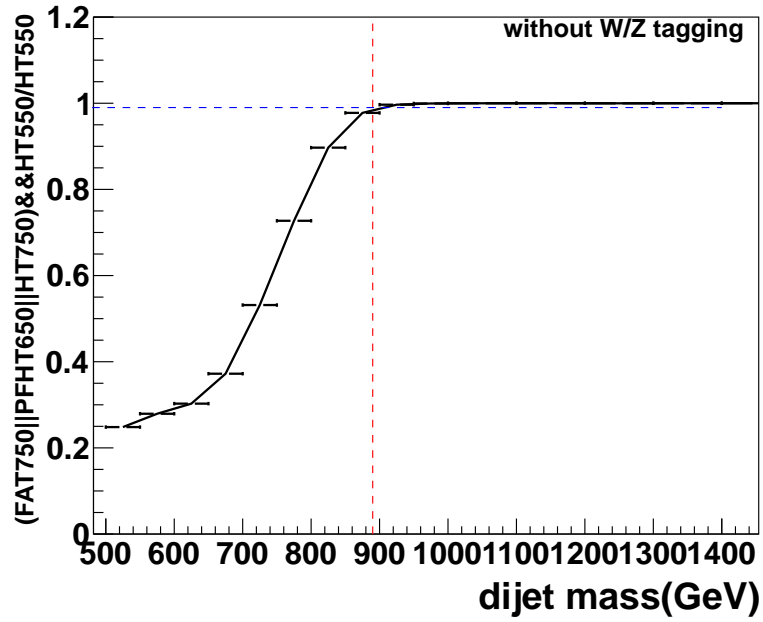
Figure 3.4: Trigger efficiency for untagged data of FAT_750‖HLT_PF(NoPU)HT650‖HLT_HT750 measured using data collected by lower threshold $H_T 550$ trigger. The dash red line is positioned at m_{jj} equal $890 GeV$, the blue line is at efficiency at 99%.
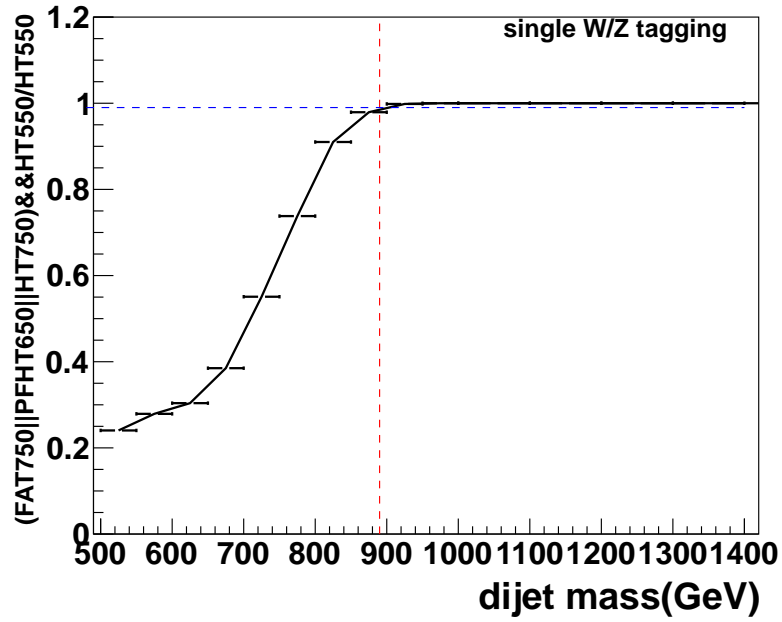
Figure 3.5: Trigger efficiency for single tagged data of FAT_750‖HLT_PF(NoPU)HT650‖HLT_HT750 measured using data collected by lower threshold $H_T 550$ trigger. The dash red line is positioned at m_{jj} equal $890 GeV$, the blue line is at efficiency at 99%.
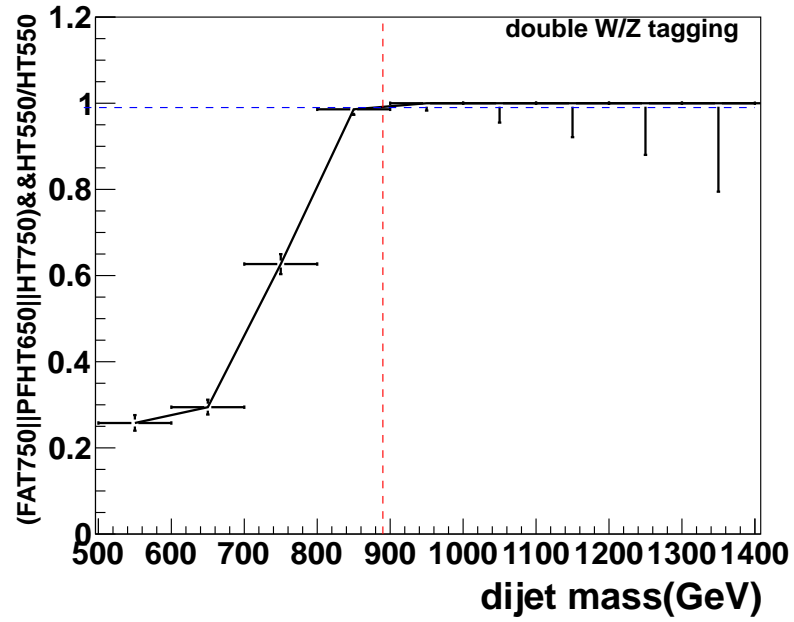
Figure 3.6: Trigger efficiency for double tagged data of FAT_750‖HLT_PF(NoPU)HT650‖HLT_HT750 measured using data collected by lower threshold $H_T 550$ trigger. The dash red line is positioned at m_{jj} equal $890 GeV$, the blue line is at efficiency at 99%.

3.6 Data and MC comparisons

In this section, we compare some kinematic features of the jets between QCD MC and data, which are shown in Fig 3.7, 3.8,3.9, 3.10, 3.11, 3.12,3.13, 3.14, 3.15, 3.16, 3.17, 3.18, 3.19, 3.20, 3.21, and 3.22. Predictions from Pythia6 with Tune $Z2*$ and Herwig++ with Tune 23 are shown. The comparison is shown in the exclusive dijet category, low and high purity, single and double tagged events.. The distributions are shown after the event selection (in particular $|y| < 2.5$, $|\Delta\eta| < 1.3$, $m_{jj} > 890 GeV$) is applied. The number of data events in each mass bin are shown in Table 3.6. The MC is normalized to the number of data events in each category and the shapes are compared.
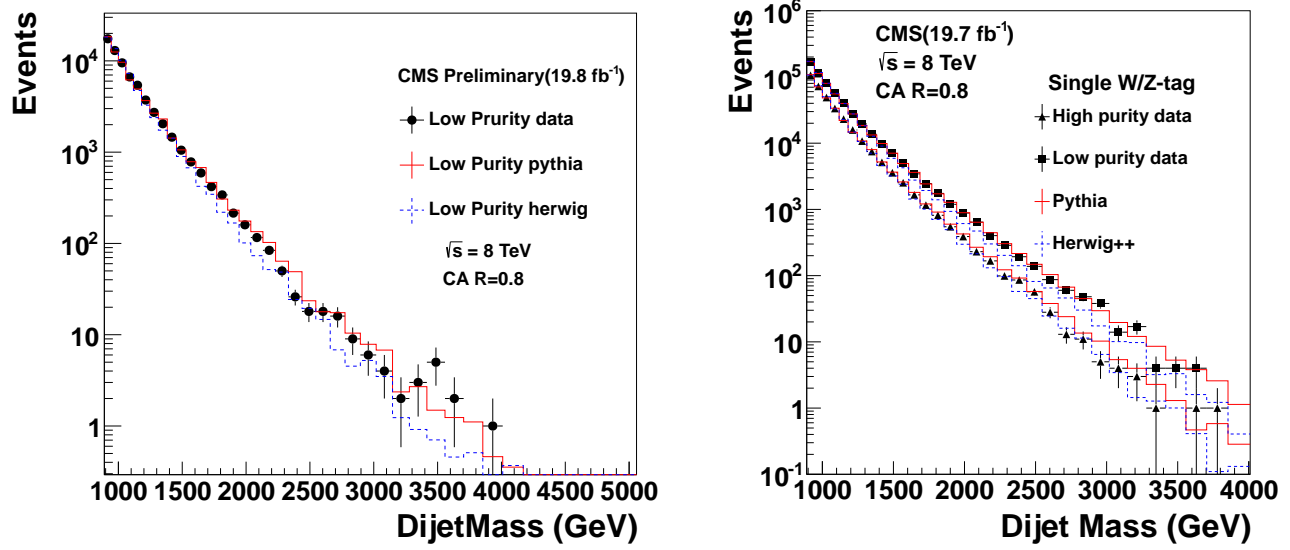
Figure 3.7: Comparisons between data and Monte Carlo for invariant mass of the two leading jets of low purity (left) and low-high purity (right) 1-tagged events. The MC is normalized to the number of data events in each category.
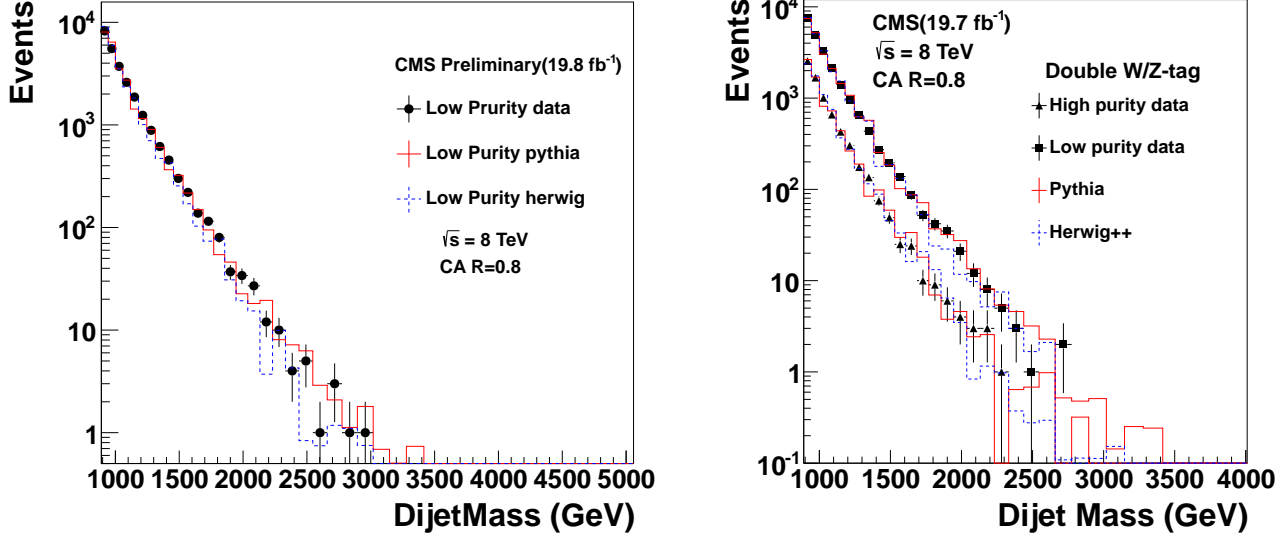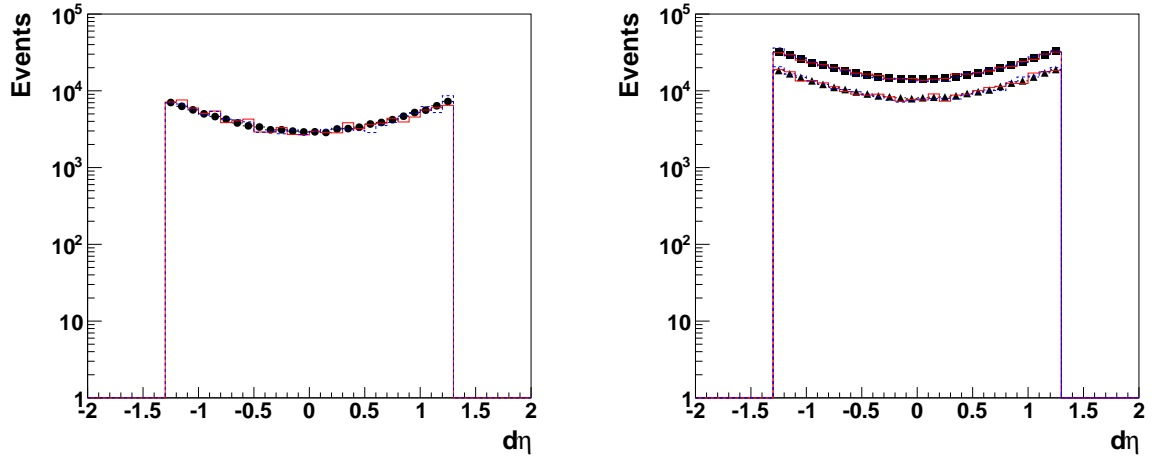
Figure 3.8: Comparisons between data and Monte Carlo for invariant mass of the two leading jets of low purity (left) and low-high purity (right) 2-tagged events. The MC is normalized to the number of data events in each category.

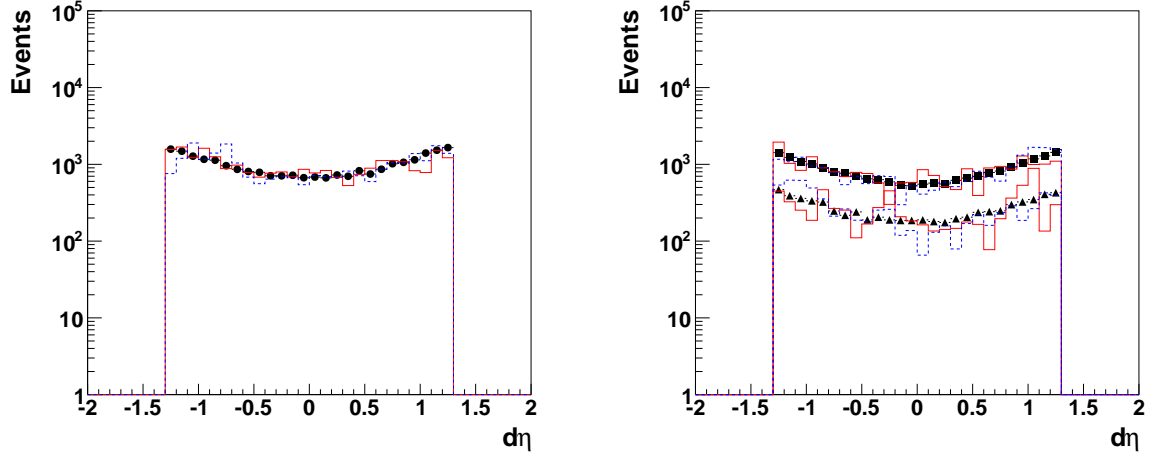

Figure 3.9: Comparisons between data and Monte Carlo for $\Delta\eta$ of the two leading jets of low purity (left) and low-high purity (right) 1-tagged events. The MC is normalized to the number of data events in each category.

lower mass bin border	low purity 1-tag events	high purity 1-tag events	low purity 2-tag events	high purity 2-tag events
890	165671	105892	7586	2544
944	115622	72007	4950	1673
1000	80537	48930	3311	1005
1058	56423	33398	2159	658
1118	39817	23086	1407	427
1181	27651	15817	962	302
1246	19531	10741	647	175
1313	13617	7477	434	135
1383	9880	5128	272	75
1455	6992	3578	195	49
1530	4939	2525	138	25
1607	3443	1658	86	24
1687	2454	1160	52	10
1770	1744	815	42	9
1856	1193	547	35	6
1945	881	389	21	4
2037	643	230	12	3
2132	402	167	8	3
2231	287	99	5	1
2332	193	86	3	
2438	138	57	1	
2546	87	28	0	

Figure 3.10: Comparisons between data and Monte Carlo for $\Delta\eta$ of the two leading jets of low purity (left) and low-high purity (right) 2-tagged events. The MC is normalized to the number of data events in each category.
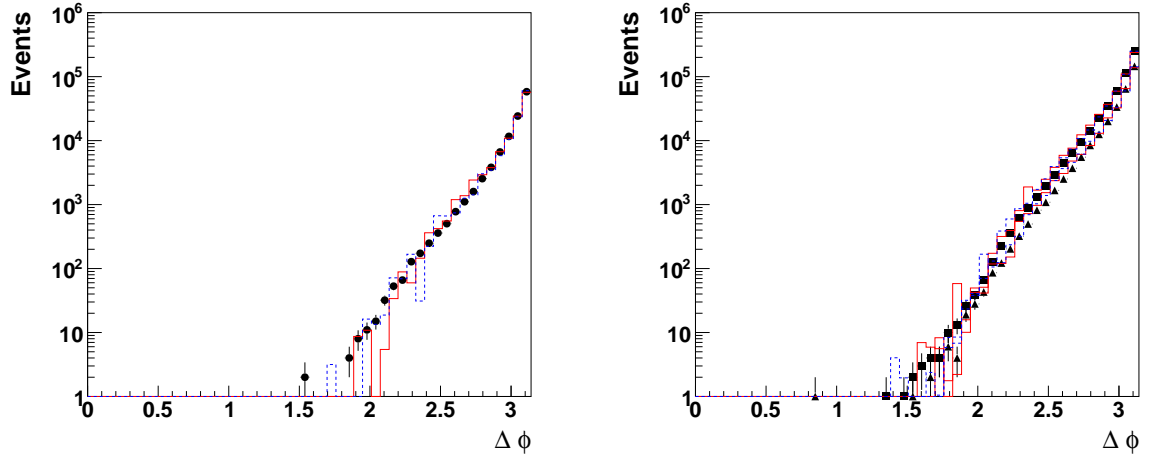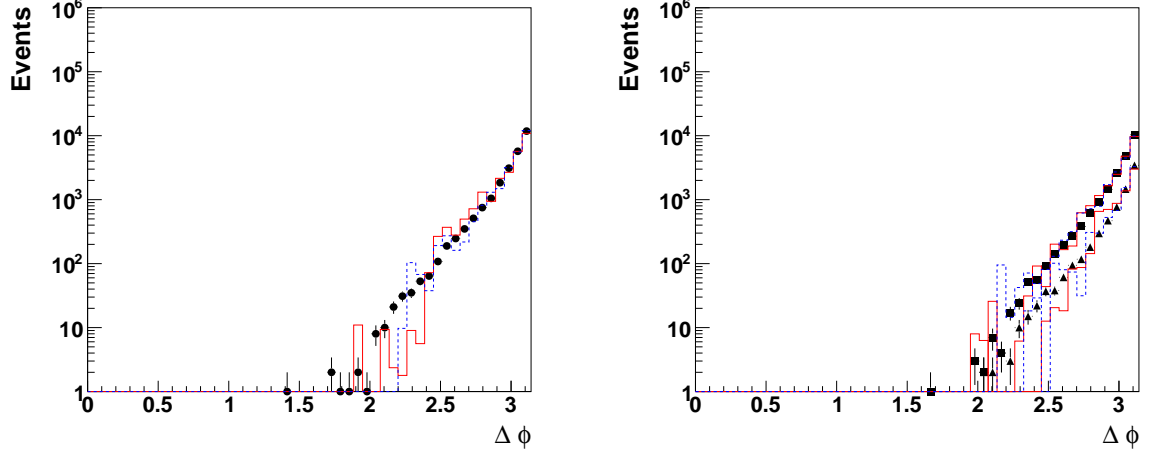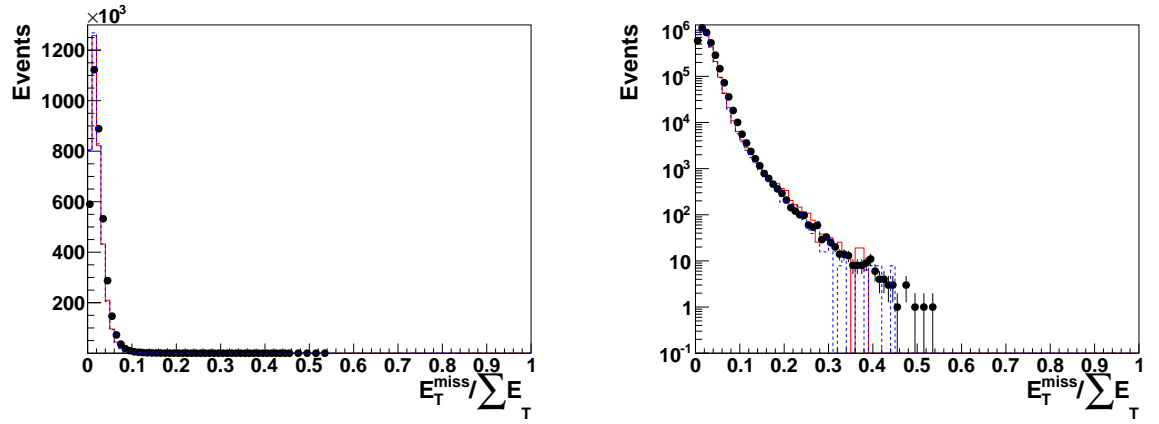

Figure 3.11: Comparisons between data and Monte Carlo for $\Delta\phi$ of the two leading jets of low purity (left) and low-high purity (right) 1-tagged events. The MC is normalized to the number of data events in each category.

Figure 3.12: Comparisons between data and Monte Carlo for $\Delta\phi$ of the two leading jets of low purity (left) and low-high purity (right) 2-tagged events. The MC is normalized to the number of data events in each category.

Figure 3.13: Comparisons between data and Monte Carlo for $E_T^{miss}/\sum E_T$ The MC is normalized to the number of data events. Plot on the right is the log scale plot. (The plot includes only a subset of the full data sample.)
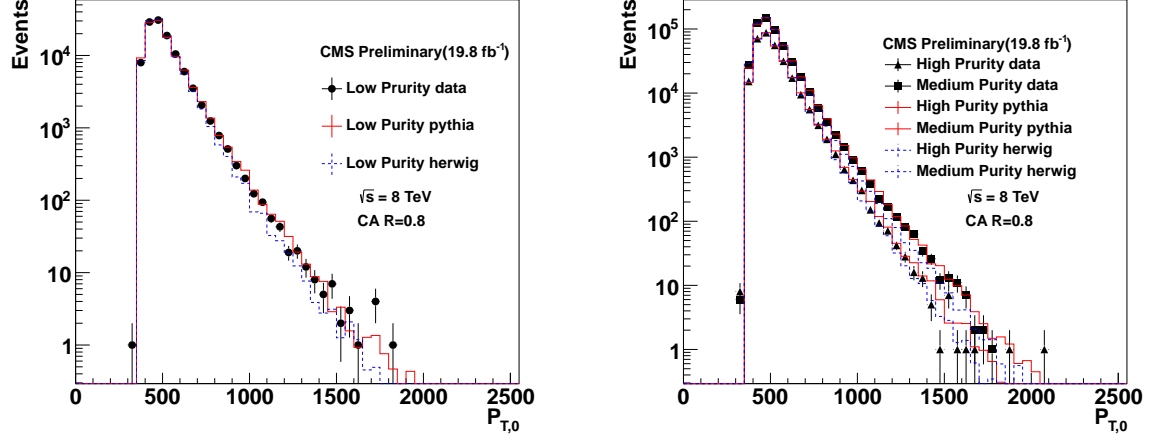
Figure 3.14: Comparisons between data and Monte Carlo for p_T of the leading jet of low purity (left) and low-high purity (right) 1-tagged events. The MC is normalized to the number of data events in each category.
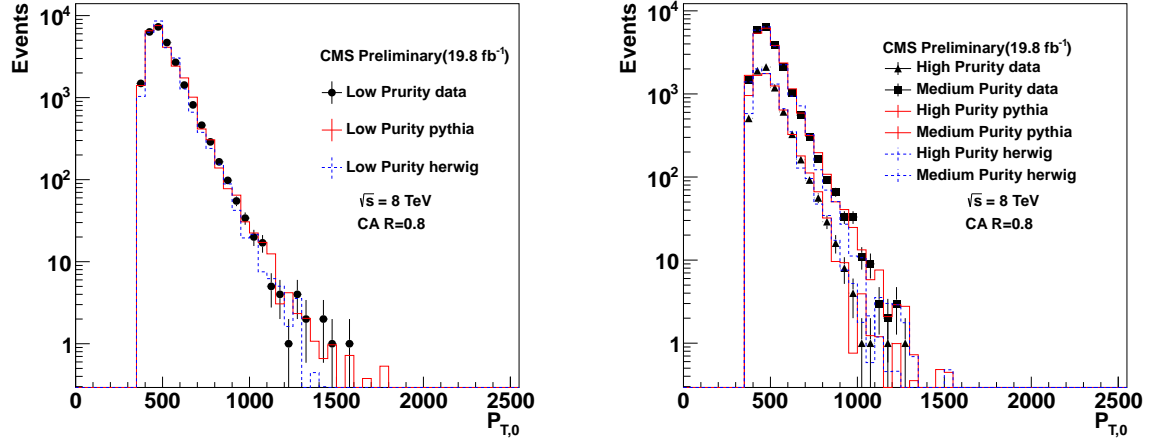

Figure 3.15: Comparisons between data and Monte Carlo for p_T of the leading jet of low purity (left) and low-high purity (right) 2-tagged events. The MC is normalized to the number of data events in each category.
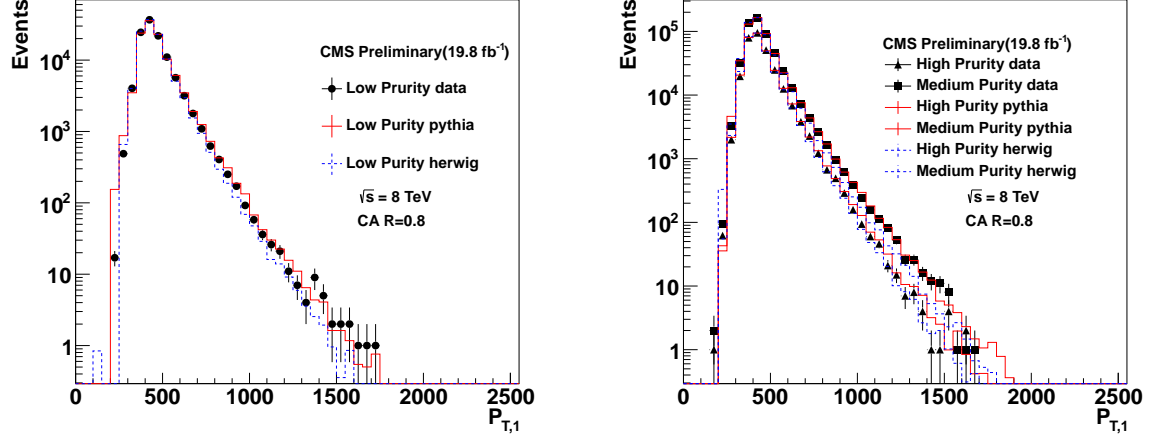
Figure 3.16: Comparisons between data and Monte Carlo for p_T of the second leading jet of low purity (left) and low-high purity (right) 1-tagged events. The MC is normalized to the number of data events in each category.

Figure 3.17: Comparisons between data and Monte Carlo for p_T of the second leading jet of low purity (left) and low-high purity (right) 2-tagged events. The MC is normalized to the number of data events in each category.
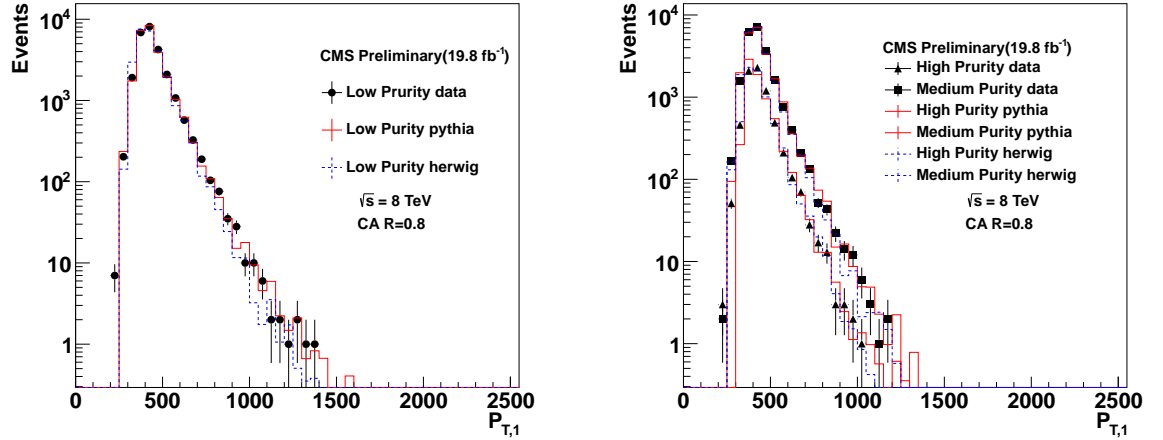
Figure 3.18: Comparisons between data and Monte Carlo for η of the leading jet of low purity (left) and low-high purity (right) 1-tagged events. The MC is normalized to the number of data events in each category.
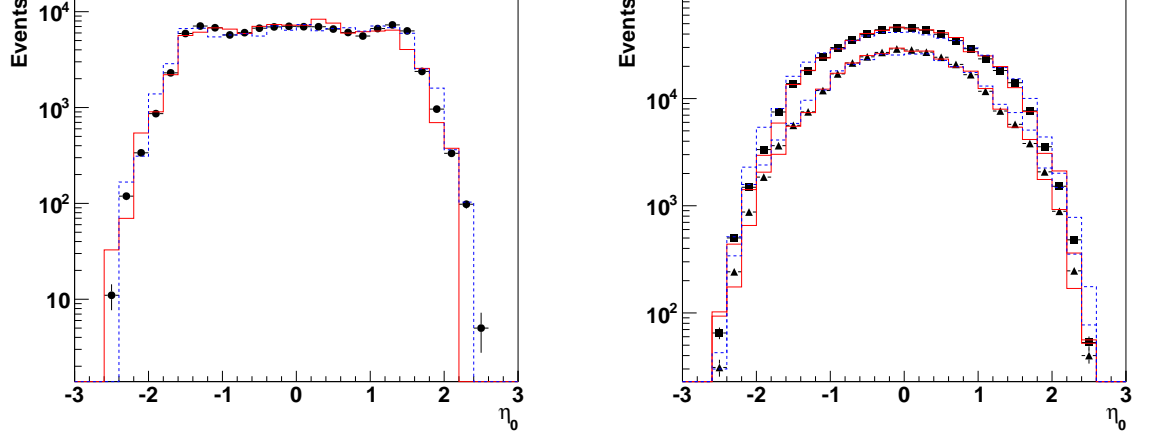

Figure 3.19: Comparisons between data and Monte Carlo for η of the leading jet of low purity (left) and low-high purity (right) 2-tagged events. The MC is normalized to the number of data events in each category.

Figure 3.20: Comparisons between data and Monte Carlo for η of the second leading jet of low purity (left) and low-high purity (right) 1-tagged events. The MC is normalized to the number of data events in each category.
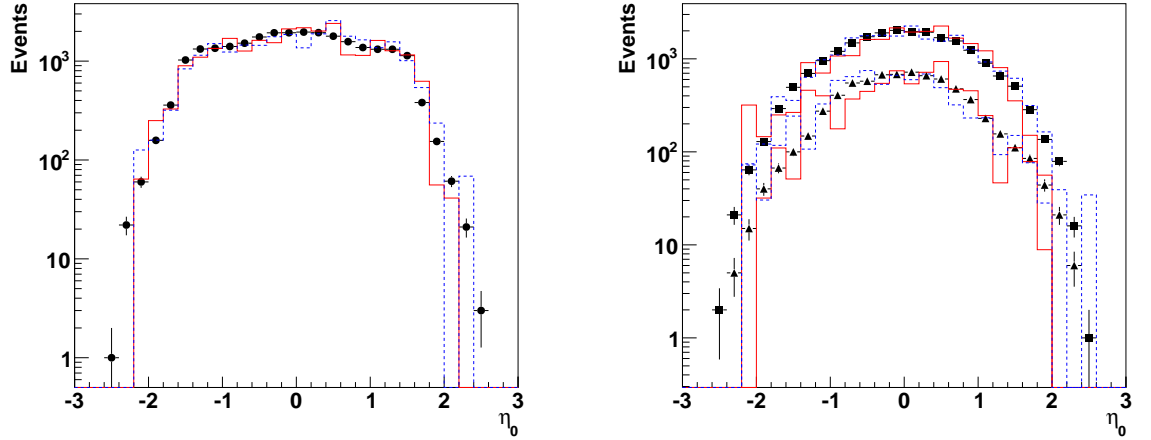

Figure 3.21: Comparisons between data and Monte Carlo for η of the second leading jet of low purity (left) and low-high purity (right) 2-tagged events. The MC is normalized to the number of data events in each category.
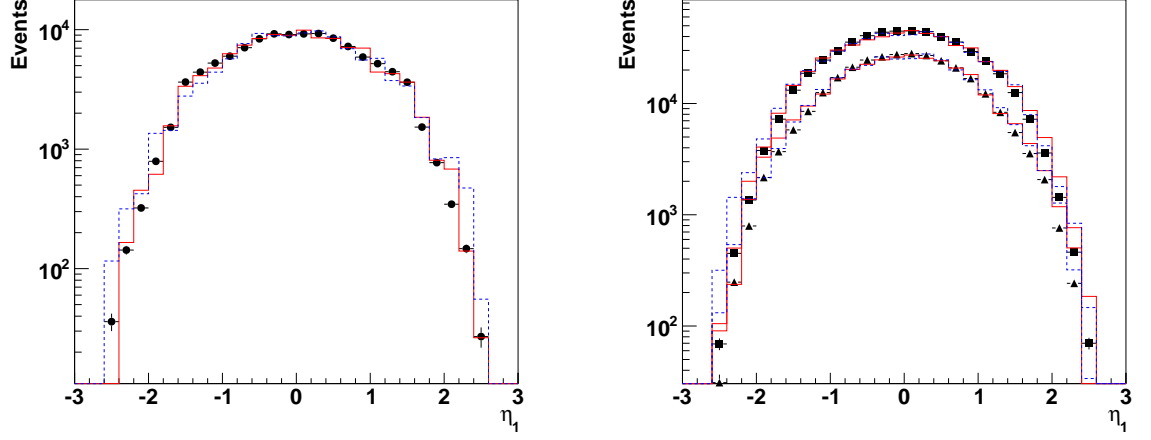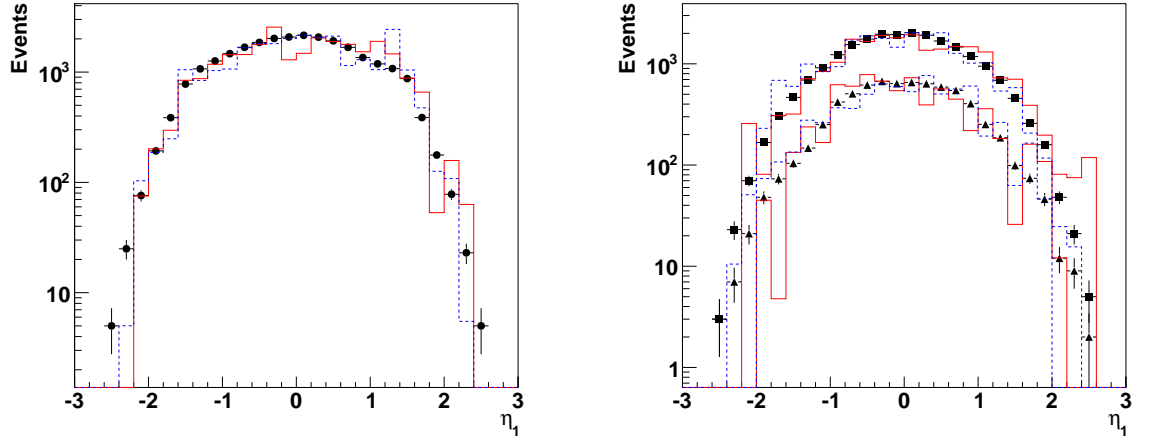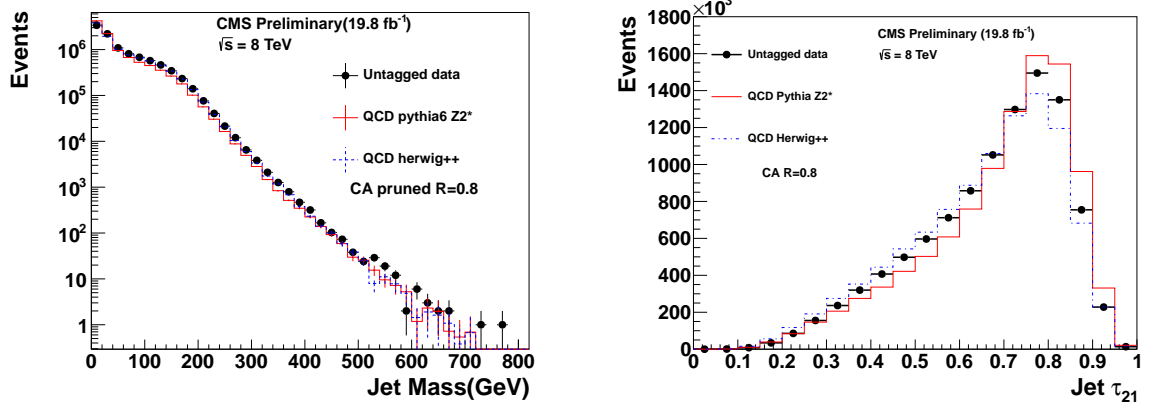
Figure 3.22: Comparisons between data and Monte Carlo for mass(left) and τ_{21}(right) of the leading two jets. The MC is normalized to the number of data events in each category.
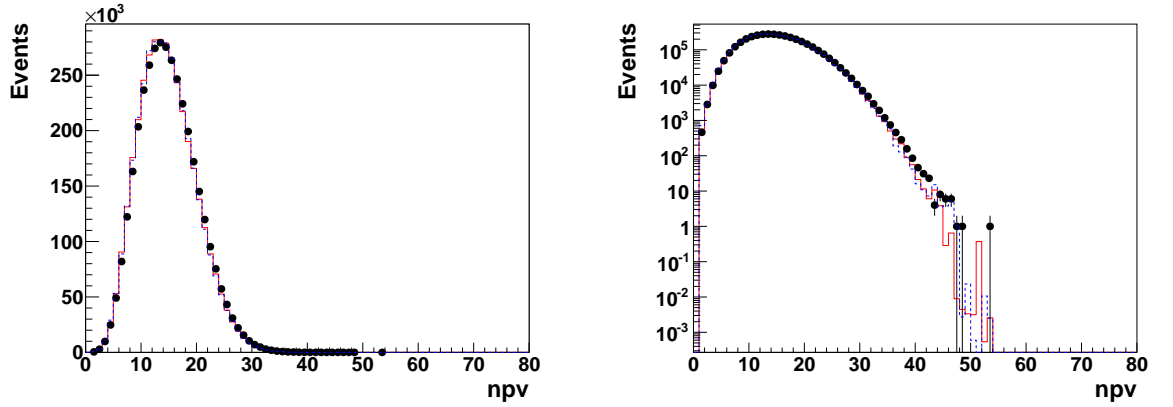
Figure 3.23: Comparisons between data and Monte Carlo for number of primary vertice to show the effect on Monte Carlo after pile up reweighting. The MC is normalized to the number of data events. Plot on the right is the log scale plot. (The plot includes only a subset of the full data sample.)

Figure 3.24: Comparisons between data and Monte Carlo for neutral hadron energy fraction. The MC is normalized to the number of data events. Plot on the right is the log scale plot. (The plot includes only a subset of the full data sample.)

Figure 3.25: Comparisons between data and Monte Carlo for neutral eletromagnetic energy fraction. The MC is normalized to the number of data events. Plot on the right is the log scale plot. (The plot includes only a subset of the full data sample.)
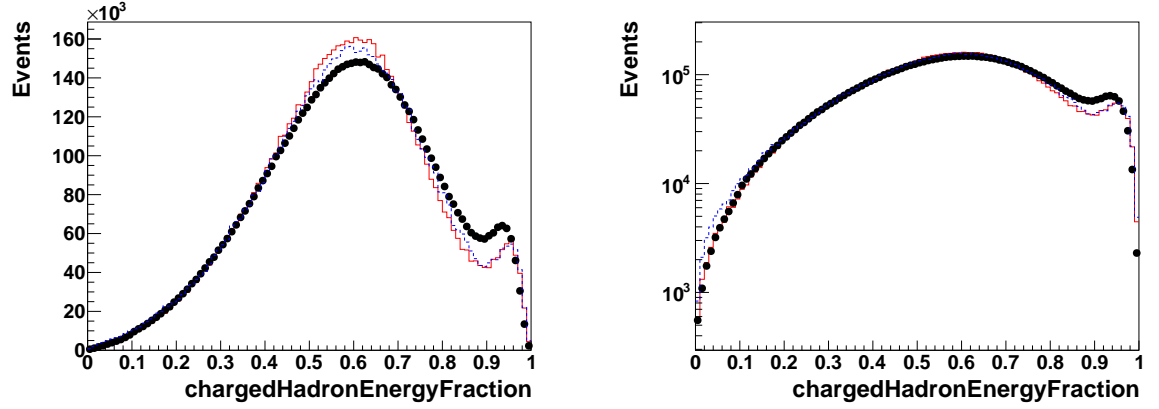
Figure 3.26: Comparisons between data and Monte Carlo for charged hadron energy fraction. The MC is normalized to the number of data events. Plot on the right is the log scale plot. (The plot includes only a subset of the full data sample.)
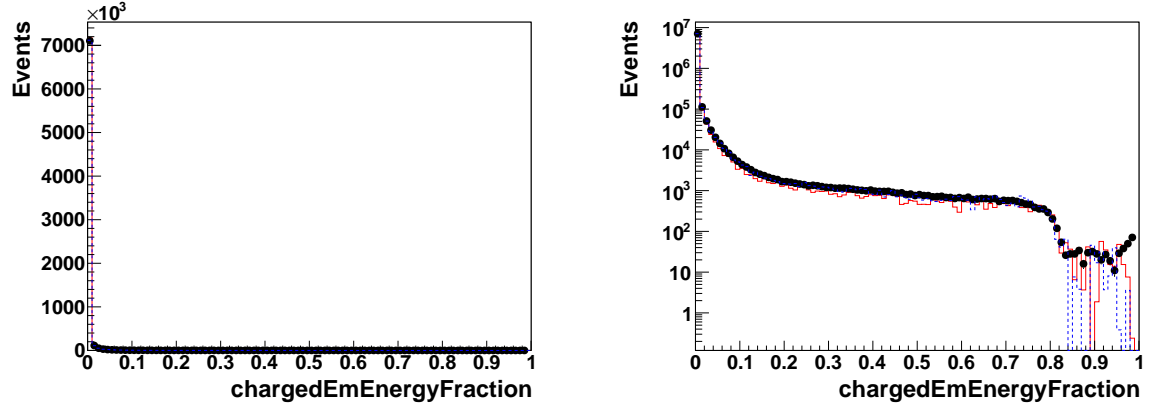
Figure 3.27: Comparisons between data and Monte Carlo for charged eletromagnetic energy fraction. The MC is normalized to the number of data events. Plot on the right is the log scale plot. (The plot includes only a subset of the full data sample.)
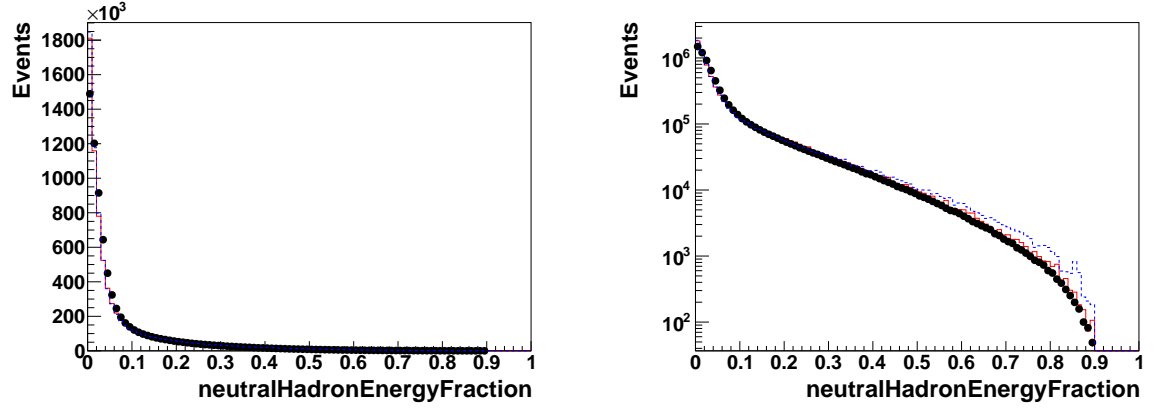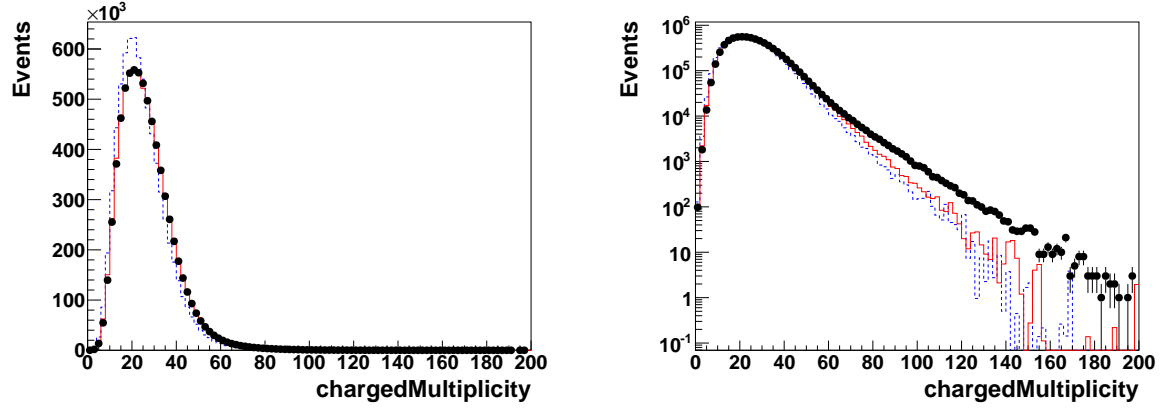
Figure 3.28: Comparisons between data and Monte Carlo for charged multiplicity. The MC is normalized to the number of data events. Plot on the right is the log scale plot. (The plot includes only a subset of the full data sample.)
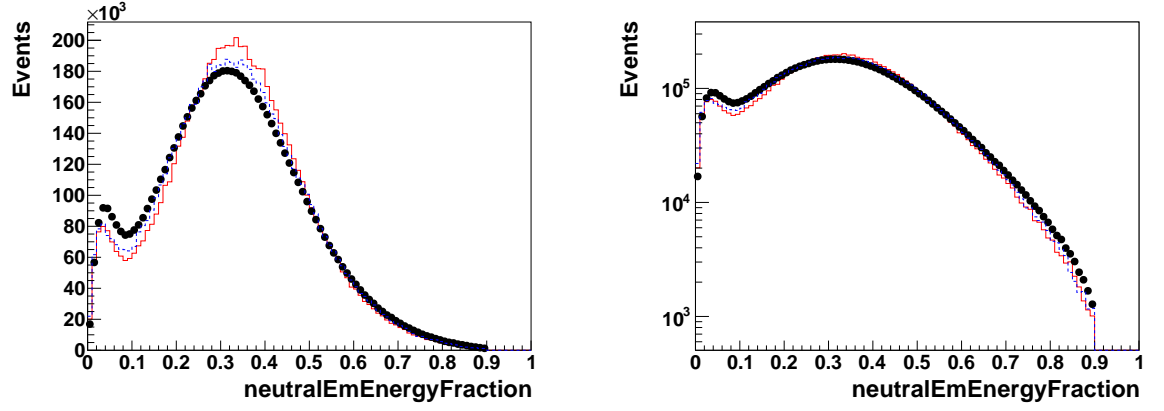

Figure 3.29: Comparisons between data and Monte Carlo for number of constituents. The MC is normalized to the number of data events. Plot on the right is the log scale plot. (The plot includes only a subset of the full data sample.)
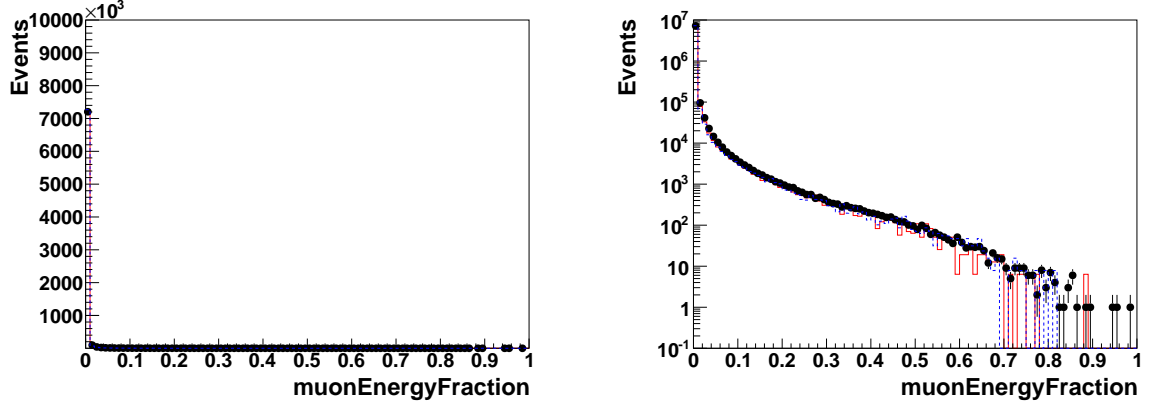
Figure 3.30: Comparisons between data and Monte Carlo for the muon energy fraction of the leading two jets. The MC is normalized to the number of data events. Plot on the right is the log scale plot. (The plot includes only a subset of the full data sample.)
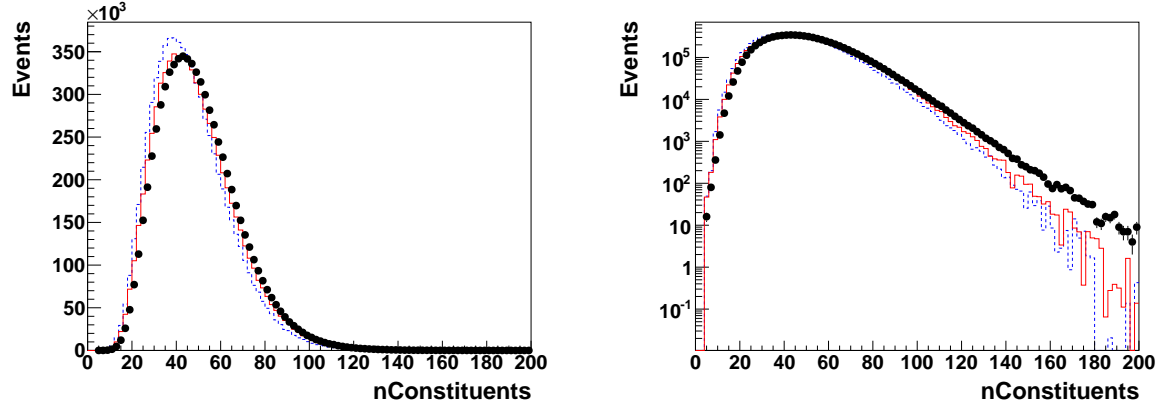
We find that the QCD MC agrees with data, although not perfect. For the dijet kinematics and also the jet substruture variables, we observe about the same agreement of Pythia6 $Z2*$ and Herwig++. For this analysis, we chose to model the background shape from the data itself (as described below) and depend on QCD MC only to provide us guidance and a cross check.

Fig 3.11, Fig 3.12 and Fig 3.13 are particulariy useful to identify jets from calorimenter noise which would show up at low values of $\Delta\phi$ and high values of $E_T^{miss}/\sum E_T$. No enhencement in this region is observed which gives confidence that the applied noise filter cleaning and jet ID cuts leave no noise contamination within the two leading jets.

Fig 3.23 shows the number of primary vertices distribution after pile up reweighting on the MC. Fig 3.24, Fig 3.25, Fig 3.26, Fig 3.27, Fig 3.28 and Fig 3.29 show the

jet ID variable distribution after the event selection, and Fig 3.30, the muon energy

faction of the leading two jets.

3.7 W-tagging scale factor

We derive the scale factor for the $\tau2/\tau1$ W tagger, in both the tight and loose regions, by comparing its efficiency in semileptonic $t\bar{t}$ events, both in data and mote carlo. We isolate the W candidates with kinematic cuts. We consider only muon events. We then apply the tagger and require the W mass to be within 70 and 100 GeV.

In Monte Carlo, we attempt to match the CA8 jets to real Ws by requiring that the daughters of a hadronic W from the particle generator lie within a cone of $\Delta R < 0.3$ of a jet's subjets. Jets that meet this requirement are "matched" jets. We can then classify all W candidates in the following ways:

1. Matched W jets which pass the tight $\tau2/\tau1$ cut.

2. Matched W jets which pass the loose $\tau2/\tau1$ cut.

3. Matched W jets which fail both $\tau2/\tau1$ cuts.

4. Unmatched W jets which pass the tight $\tau2/\tau1$ cut.

5. Unmatched W jets which pass the loose $\tau2/\tau1$ cut.

6. Unmatched W jets which fail both $\tau2/\tau1$ cuts.

The efficiency for either tight or loose can be extracted by counting the number of matched W jets in that region and dividing by the total number of matched W jets.

We derive the efficiency in data by simultaneously fitting the W mass distributions of the events in the tight, loose and failed events. The general shapes of the distributions are taken from MC. The efficiencies are explicit fit parameters which relate the normalizations of categories category. We must also take into account small background contributions from non-$t\bar{t}$ sources. These contributions are also parametrized as shapes and included in the fit.

3.7.1 Fit to Monte Carlo

We first find the PDFs associated with each of the event categories above by fitting their distributions from the Monte Carlo, as follows:

- **Tight, Matched Jets** We fit the tight matched events with the sum of two gaussians.

- **Loose, Matched Jets** We fir the loose matched events with a sum of the double-gaussian found in the tight selection and an exponential.

- **Failed, Matched Jets** We fit failed matched events with an exponential.

- **Tight, Unatched Jets** We fit tight unmatched events with the sum of a gaussian and a linear function with positive slope.

- **Loose, Unatched Jets** We fit loose unmatched events with a gaussian.

- **Failed, Unatched Jets** We fit failed unmatched events with an exponential.

- **Backgrounds** All backgrounds are fit with gaussians in the tight and loose regions, and an exponential in the failed region. These shapes are added to the respective unmatched shapes to derive a total non-matched shape.

Fits to matched and unmatched distributions are shown in figures 3.31 and 3.32.
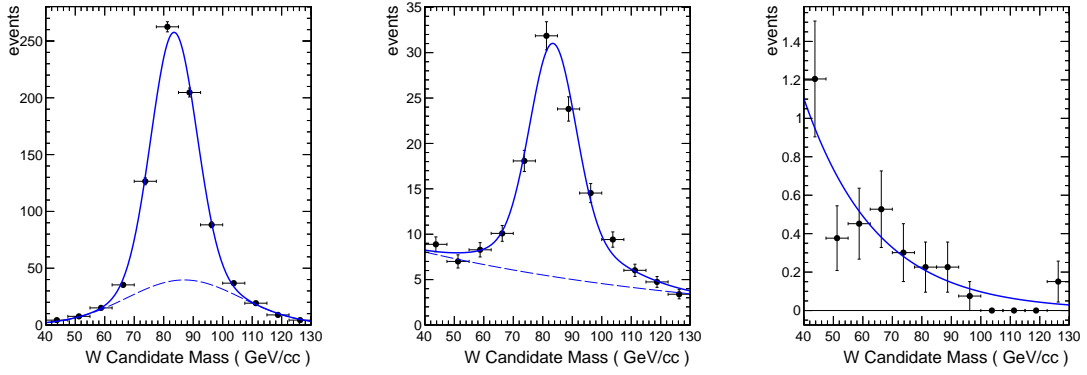

Figure 3.31: Fits to matched $t\bar{t}$ distributions. Left: tight region. Center: loose region. Right: failed events.
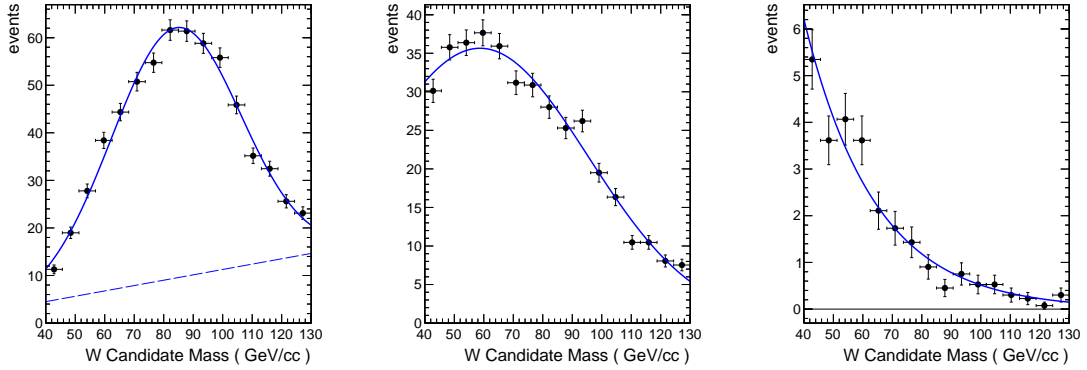
Figure 3.32: Fits to unmatched $t\bar{t}$ distributions. Left: tight region. Center: loose region. Right: failed events.

78

3.7.1.1 Fits to Data

We fit the above shapes to the data. The following parameters are kept constant, with their values taken form the MC fits described in the previous section:

1. In the unmatched and background distrubtions

   (a) The relative normalization of the gaussian and linear components of the tight, unmatched shape.

   (b) The position of the gaussian peak in the loose, unmatched distribution is fixed.

   (c) The means and standard deviations, as well as the decay coefficients of all backgrounds are fixed, but their normalizations are not.

2. In the matched distributions

   (a) The relative normalization of the two gaussians in the tight region is fixed.

   (b) The relative position (as a multiplier) of the two gaussian peaks is fixed.

   (c) The relative normalization of the exponential and double-gaussian shapes in the loose region is fixed.

All other parameters are allowed to float. All other normalizations are parametrized in terms of the efficiency. The results of the fits to data are shown in figure 3.33. As a consistency check, the same proceedure is applied to the MC distribution. The result of that fit is shown in figure 3.34.
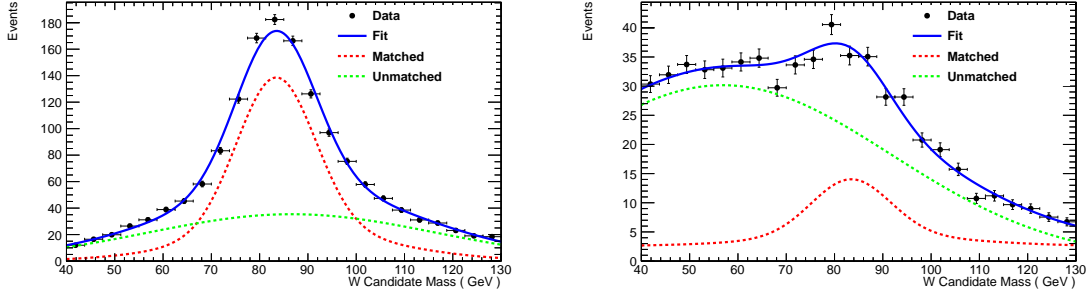
Figure 3.33: Distributions from data of W mass in the tight (left) and loose (right) τ_2/τ_1 regions, and resulting fits.
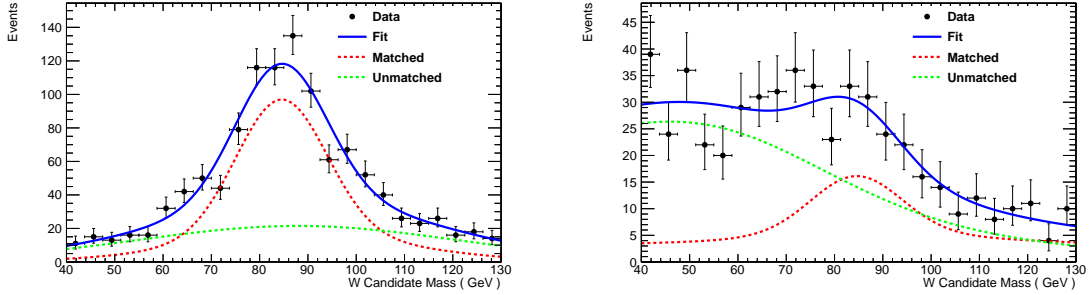
Figure 3.34: Distributions from MC of W mass in the tight (left) and loose (right) τ_2/τ_1 regions, and resulting fits.

More details on the fitting procedure and the $t\bar{t}$ selection can be found in the appendix of this note.

3.7.2 Scale Factor Measurement

We measure the scale factor of the $\tau 2/\tau 1$ cut efficiency and that of the W mass window 70 to $100 GeV$ efficiency. We find that the total scale factor for the two cuts is 0.860 ± 0.065 in the tight region and 138.5 ± 75.2 in the loose region.

3.7.2.1 Systematics

The errors in the scale factors are found from the fitting errors and systematic errors from the choice of fixed parameters. Each fixed parameter found in MC is varied by its fitting error and used to generate toy MC to which the fitting proceedure is applied. The resulting offset is taken to be the systematic error from this fixed parameter. In addition, when the efficiency from a fit to MC differs with that from MC truth information, we take the difference to be an additional systematic. Additional systematic uncertainties on the W-tagging efficiency related to detector effects are discussed in the systematics section of this note.

3.8 The signal: dijet resonance

We search for dijet resonances corresponding to several models. Using the W/Z-tagging algorithm, we examine both single W/Z-tag and double W/Z-tag events.

The pruned jet mass and jet τ_{21} distributions in signal MC, data and background MC are shown in Fig. 3.35. Fully merged jets from Ws and Zs peak around 80-90 GeVin pruned jet mass while QCD jets and not fully merged Ws and Zs peak around 20 GeV. The discriminating power of the pruned jet mass and τ_{21} for the different signals is evident.

For both the pruned jet mass and τ_{21}, differences are observed between the HER-WIG++ (G_{RS}) and PYTHIA6 (G_{Bulk}, q^*, W') distributions, which arise from differences in the polarization of the W/Z boson and the showering and hadronization models used by these generators. In particular this is the reason why the WZ prediction for τ_{21} is different from the WW, ZZ predictions. The differences due to showering and hadronization models are into account in the estimate of the systematic uncertainties on the tagging efficiency, as discussed below.

The full event selection efficiency is estimated using simulated signal samples. Less than 1% of the ZZ or WW events which pass the full selection are from $ZZ \to llqq$ or $WW \to l\nu qq$ decays, where l can be a muon or electron. While 3% of the selected ZZ events are from $ZZ \to \tau\tau qq$ decays, less than 1% of the selected WW events are from $WW \to \tau\nu qq$ decays. To within 10% accuracy the full selection efficiency can therefore be approximated by the product of the W/Z-tagging efficiency and an
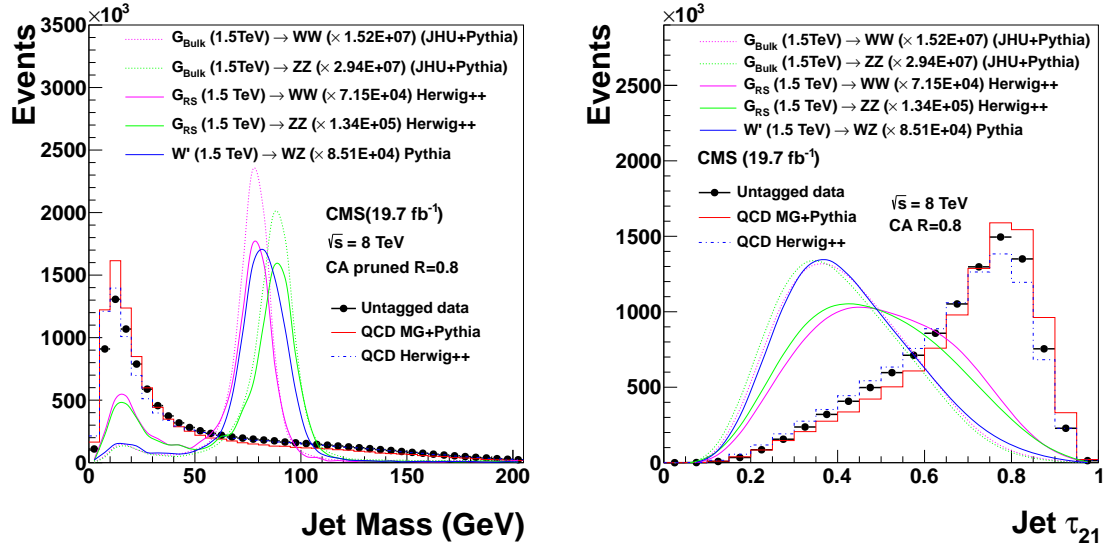
Figure 3.35: Pruned jet mass and τ_{21} in signal MC, data and background MC. All curves are plotted with the same binning. The signal MC distributions are plotted as smooth curves connecting the histogram entries. MC are normalized according to data.

approximate acceptance. This acceptance is shown in Fig. 3.36 and takes into account the angular acceptance ($|\eta| < 2.5$, $|\Delta\eta| < 1.3$), the branching into quark final states, BR($W/Z \to$ quarks) and a matching within $\Delta R = \sqrt{(\Delta\eta)^2 + (\Delta\phi)^2} < 0.5$ between the generated W/Z bosons and the reconstructed jets.

The W/Z-tagging efficiency is shown in Fig. 3.37 and Fig. 3.38.

The signal shapes for all five processes considered in this analysis are shown in Fig. 3.39 and Fig. 3.40. For the qW and qZ final states the shape with a single W/Z-tag required is shown, while for the other signals two W/Z-tags are required.
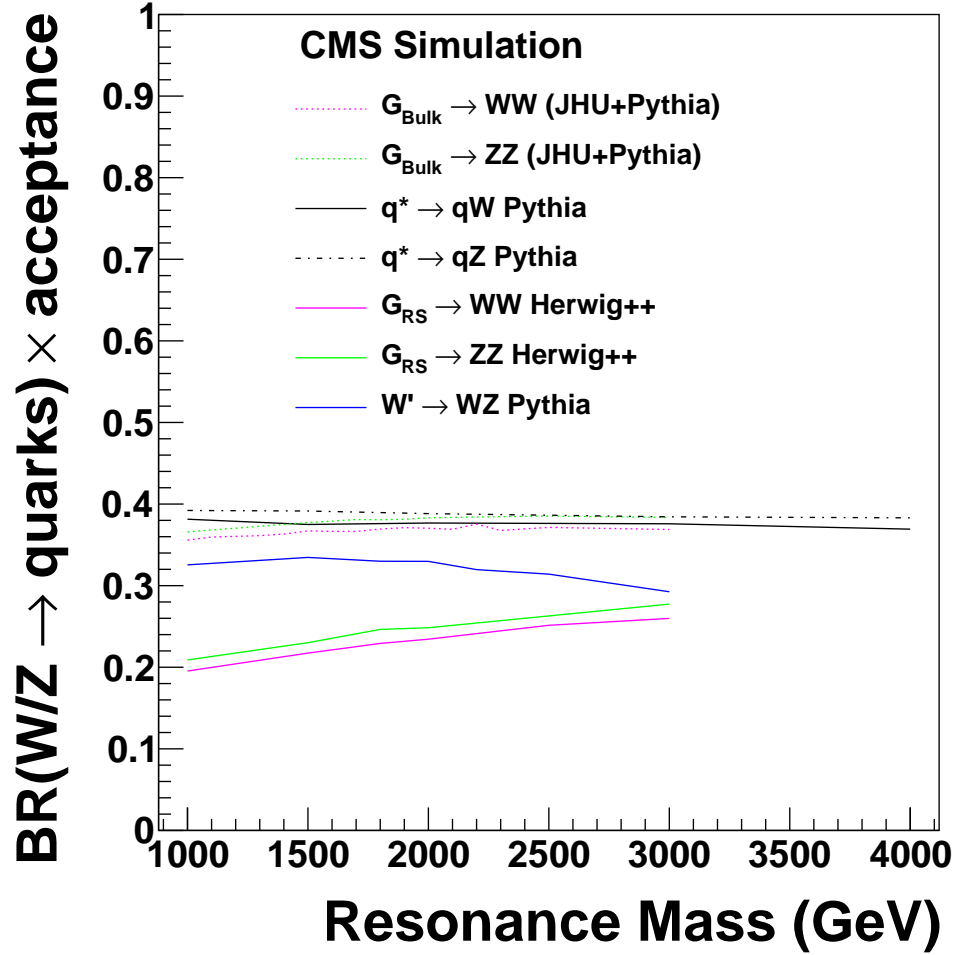
Figure 3.36: Fraction of events with branching into quark final states, BR($W/Z \to$ quarks), which are reconstructed as dijets (quarks $\to$ jets) and pass the angular acceptance ($|\eta| < 2.5$, $|\Delta\eta| < 1.3$.
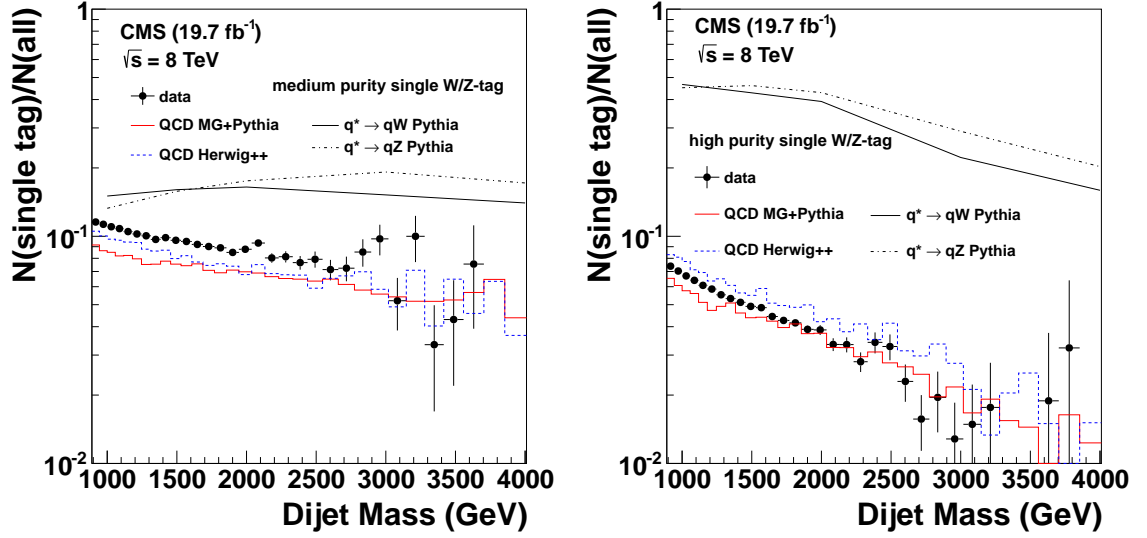
Figure 3.37: The fraction of singly-tagged events, requiring one medium purity (left) and high purity (right) W/Z-tag in data, signal and background simulations for events passing the angular acceptance requirement ($|\eta| < 2.5$, $|\Delta\eta| < 1.3$).
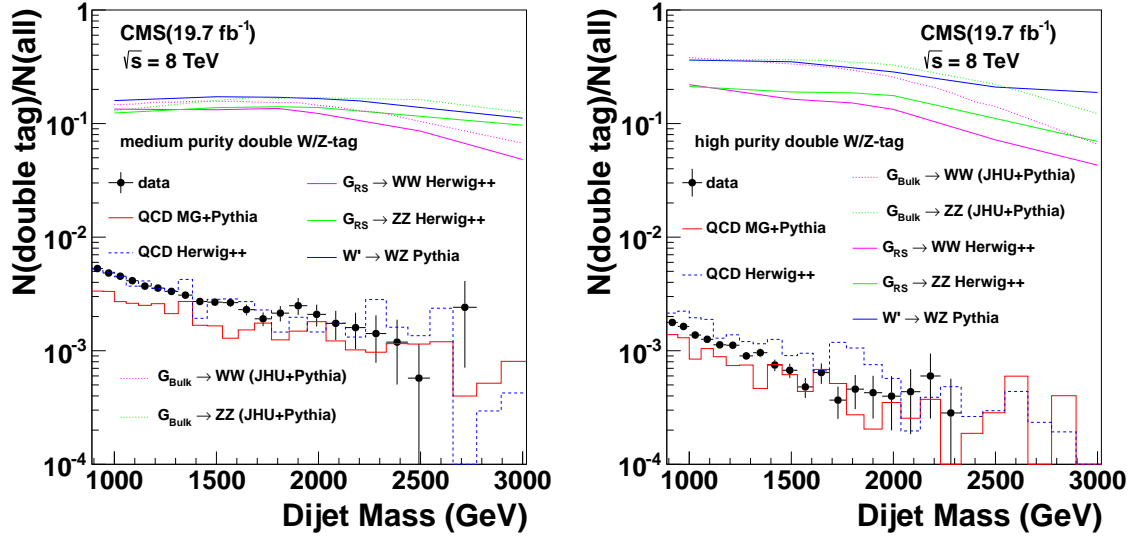
Figure 3.38: The fraction of doubly-tagged events, requiring two medium purity (left) and high purity (right) W/Z-tags in data, signal and background simulations for events passing the angular acceptance requirement ($|\eta| < 2.5$, $|\Delta\eta| < 1.3$).
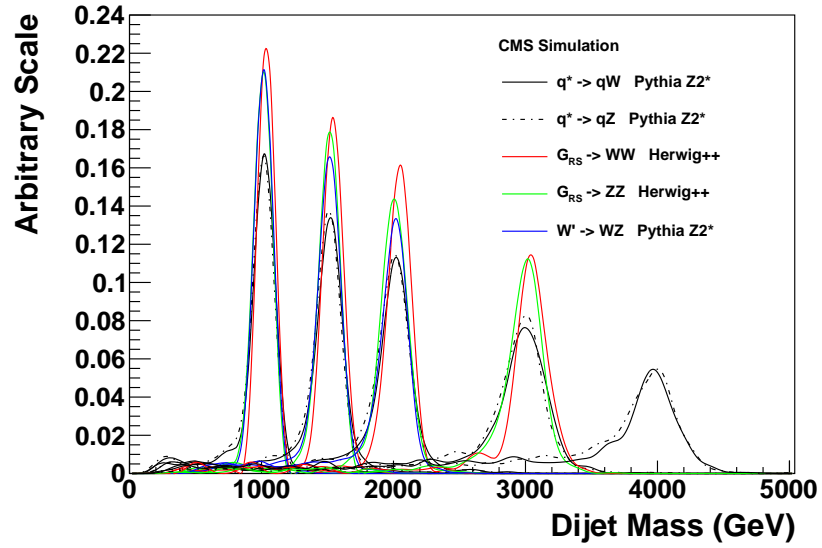
Figure 3.39: The normalized medium purity signal resonance distribution for $G_{RS} \to WW$, $G_{RS} \to ZZ$, $W' \to WZ$, $q* \to qW$, and $q* \to qZ$ resonances of dijet invariant mass 1.0TeV, 1.5TeV, 2.0TeV, 2.5 TeV, 3.0TeV, 4.0TeV.
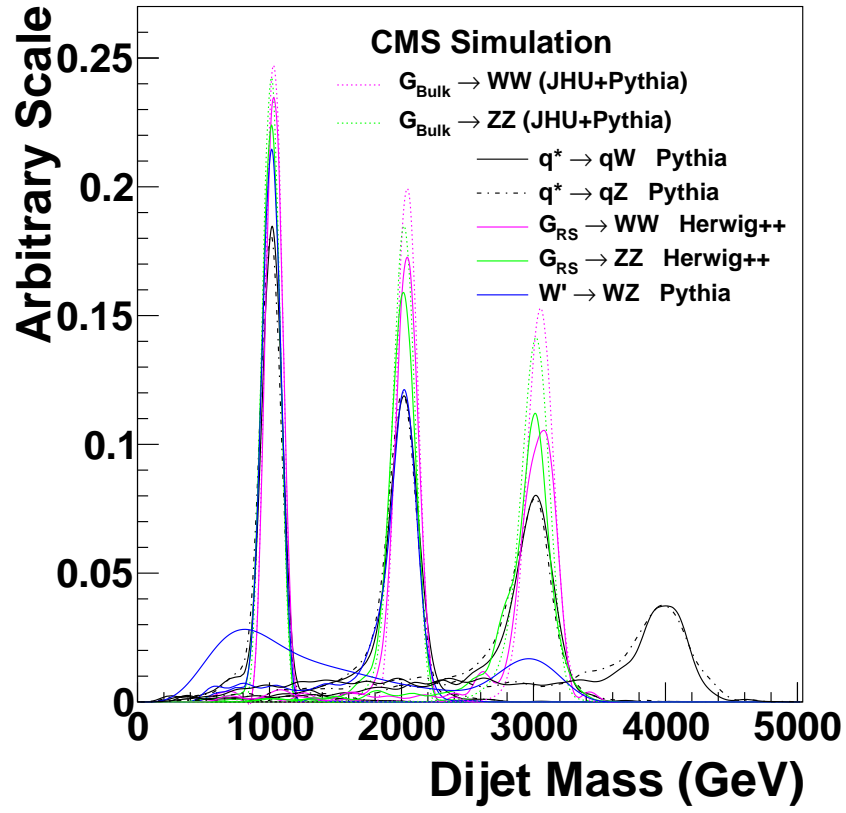
Figure 3.40: The normalized high purity signal resonance distribution for $G_{RS} \rightarrow WW$, $G_{RS} \rightarrow ZZ$, $W' \rightarrow WZ$, $q* \rightarrow qW$, and $q* \rightarrow qZ$ resonances of dijet invariant mass 1.0TeV, 1.5TeV, 2.0TeV, 3.0TeV, 4.0TeV.

3.9 Systematic uncertainties

The sources of systematic uncertainties are summarized as follows:

- Background-related systematic uncertainties: background parametrization.

- Signal-related systematics uncertainties: W/Z-tagging efficiency, Jet Energy Scale(JES), Jet Energy Resolution(JER), luminosity.

3.9.1 Background shape parametrization

We model the shape of the QCD background in the dijet spectrum using a simple parametrization which has been sucessfully deployed in previous searches in the dijet mass spectrum [59]. The background model is given in Eq. (3.1):

$$\frac{\mathrm{d}N}{\mathrm{d}m} = \frac{P_0(1 - m/\sqrt{s})^{P_1}}{(m/\sqrt{s})^{P_2}}. \tag{3.1}$$

where m denotes the dijet mass and $\sqrt{s}$ the pp center of mass energy. P_0 acts as a normalization parameter for the probability density function, and P_1, P_2 describe its shape. It was checked by a Fisher F-test that no additional parameter is not needed to discribe the distributions.

Figure 3.41 and Figure 3.42 show the dijet mass spectra from single and double W/Z-tagged data fitted to Eq. (3.1) and the bottom panes show corresponding pull distributions, demonstrating the agreement between the background-only probability

density function and the data.

No sizeable deviation from the background-only hypothesis is seen, exclusion limits are set on the product of cross section, acceptance, and branching fraction for the five considered final states: qW, qZ, WW, WZ, and ZZ.

Figure 3.41: The medium purity (left) and high purity (right) single W/Z-tagged m_{jj} distributions (points) in data fitted with the QCD background parametrization (solid curve). Signal shape distribution for $q^* \to qW$ with its corresponding cross section is also shown. Bottom panes: the corresponding pull distributions ($\frac{\text{Data}-\text{Fit}}{\sigma_{\text{Data}}}$).

3.9.2 W/Z-tagging efficiency

The W/Z-tagging efficiency is determined from the Monte Carlo simulation. We cross-check the MC modelling of the signal efficiency by measuring the W/Z-tagging efficiency in semileptonic $t\bar{t}$ data, and compare it with the same efficiency obtained using identical procedure from $t\bar{t}$ Monte Carlo sample generated with MadGraph [60]
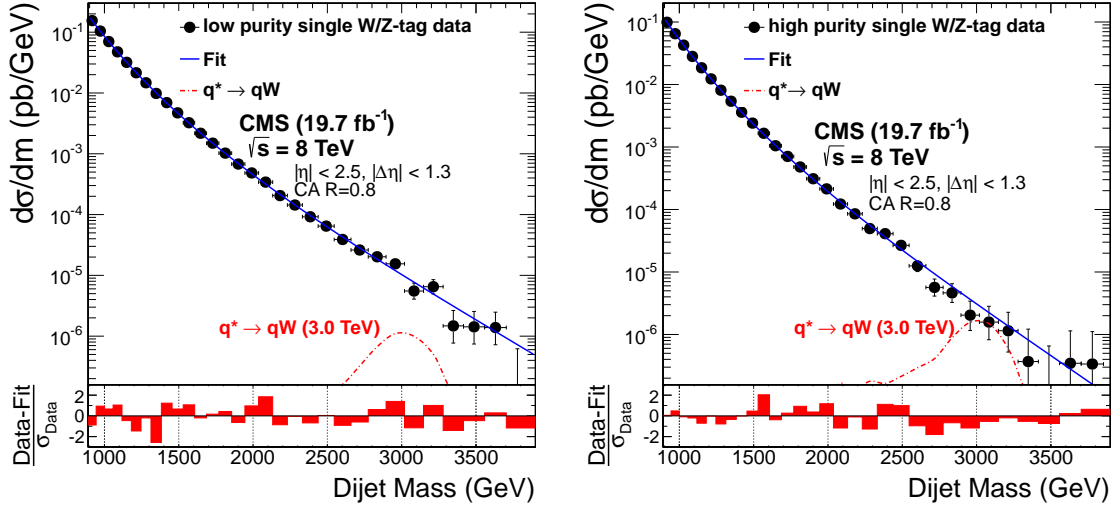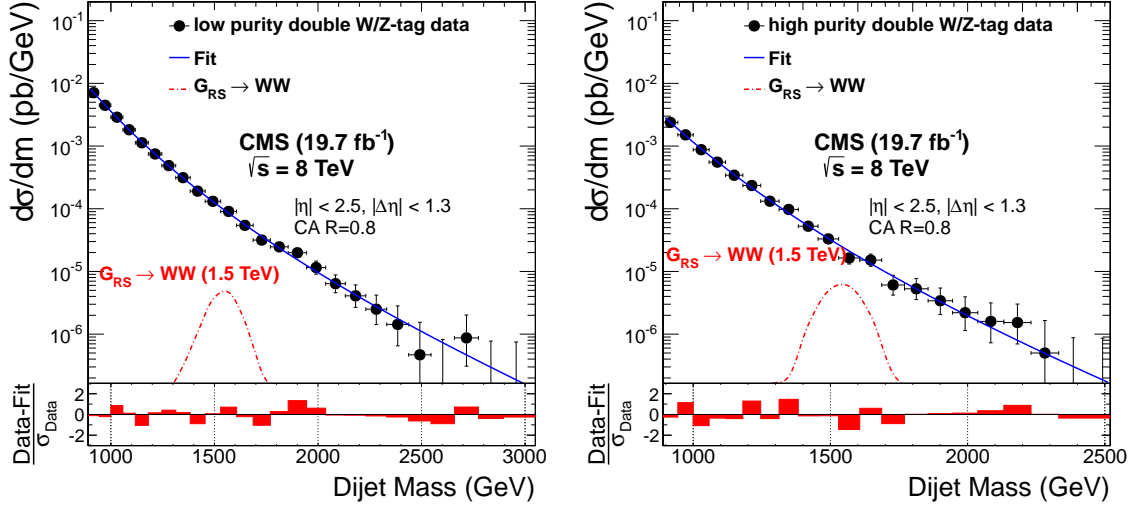
Figure 3.42: The medium purity (left) and high purity (right) double W/Z-tagged m_{jj} distributions (points) in data fitted with the QCD background parametrization (solid curve). Signal shape distribution for $G_{\mathrm{RS}} \rightarrow WW$ with its corresponding cross section is also shown. Bottom panes: the corresponding pull distributions ($\frac{\mathrm{Data} - \mathrm{Fit}}{\sigma_{\mathrm{Data}}}$).

and showered with Pythia6 Tune Z2*. The ratio of the two efficiencies defines a scale factor, which is then applied to the efficiencies for signals in the dijet data.

We follow the same procedure as described in Ref. [17]. Combining the efficiencies of the τ_{21} and jet mass cuts, a data-MC scale factor of 0.86 ± 0.07 (1.39 ± 0.75) for the high (low) purity selection for the W-tagging efficiency is determined. We assume that the same scale factor applies to Z-tagging as well. The errors on the scale factor are propagated into the systematic uncertainties on the overal signal efficiency.

The efficiency error on a single W/Z-tagging is estimated with a control sample of semileptonic $t\bar{t}$ events as described above. The uncertainties of 7.5% (54%) on the scale factors for high (low) purity tagging include sources from control sample

statistics, pruned jet mass scale and pruned jet mass resolution. Since we estimate the scale factor only in the kinematic regime of the $t\bar{t}$ sample where the W decay products merge, but the b-quarks are still reconstructed as separate jets, we need to rely on the simulation to extrapolate to higher jet p_T. Therefore, we estimate how the efficiency varies as a function of p_T for two different showering and hadronization models using G_{Bulk} samples generated with JHUGEN and interfaced with PYTHIA 6 and HERWIG++. We find that the differences are within 4% (12%) for the high (low) purity tagging and therefore smaller than the statistical uncertainty of the scale factor. Also, the dijet mass dependence of the W/Z-tagging efficiency for background events, shown in Fig. 3.37 and Fig. 3.38, is adequately described by the simulation. Other systematic errors on the tagging efficiency are small or negligible. Because of the rejection of charged particles not originating from the primary vertex and also the application of pruning, the pileup dependence on the W/Z-tagging efficiency is weak, and the uncertainty of the modeling of the pileup distribution is less than 3%. Modeling of the underlying event, estimated by switching it off in PYTHIA 6, impacts the tagging efficiency by less than 1%. These systematic errors refer to a single W/Z-tagged jet and are applied twice for double W/Z-tagged events.

3.9.3   Other uncertainties

In the jet p_T and η regions considered in this analysis, the Jet Energy Scale is known to a precision of 1-2% [48,61]. The p_T and η dependent uncertainty is propagated to

the reconstructed dijet invariant mass, resulting in an uncertainty of 1% to a good approximation independent of the reconstructed dijet invariant mass. It is taken into account by shifting the resonance dijet mass in the statistical analysis. The Jet Energy Resolution(JER) is known to a precision of 10% and its tails are in agreement between data and MC [48]. It is taken into account in the statistical analysis by a variation of the resonance width by 10%. The luminosity has been measured with an uncertainty of 2.6% [62], and is also taken into account in the statistical analysis.

3.10 Limit setting procedure

For setting upper limits on the resonance production cross section the asymptotic approximation [63] of the LHC CL_s method [64, 65] is used. The binned likelihood, L, can be written as:

$$L = \prod_i \frac{\mu_i^{n_i} e^{-\mu_i}}{n_i!} \ , \tag{3.2}$$

where

$$\mu_i = \sigma N_i(S) + N_i(B) \ , \tag{3.3}$$

n_i is the observed number of events in the ith dijet mass bin, and $N_i(S)$ is the expected number of events from the signal in the ith dijet mass bin, σ scales the signal amplitude, and $N_i(B)$ is the expected number of events from background in the ith dijet mass bin. The background $N_i(B)$ is estimated as the background component of the best signal+background fit to the data points. The dominant sources of systematic uncertainties (the jet energy scale, the jet energy resolution, the integrated luminosity, and the W/Z-tagging efficiency) are considered as nuisance parameters associated to log-normal priors. The dependence of the likelihood on their value is removed through profiling. The ratio of the profiled likelihood at a given value σ^* over the maximum of the likelihood (for $0 < \sigma < \sigma^*$) is used as a test statistics to compute the CL_s value associated to σ^*. This allows to determine the 95% confidence-level (CL) limit.

3.11   Results

The asymptotic approximation [63] of the LHC CL_s method [**?**, 64] is used to set upper limits on the cross sections for resonance production. The dominant sources of systematic uncertainties are treated as nuisance parameters associated with log-normal priors in those variables, following the methodology described in Ref. [**?**]. For a given value of the signal cross section, the nuisance parameters are fixed to the values that maximize the likelihood, a method referred to as profiling. The dependence of the likelihood on parameters used to describe the background in Eq. (3.1) is removed in the same manner, and no additional systematic uncertainty is therefore assigned to the parameterization of the background.

The HP and LP event categories are combined into a common likelihood, with the two uncertainties in the W/Z-tagging efficiencies considered to be anticorrelated between HP and LP tagging because of the exclusive selection on τ_{21}, while the remaining systematic uncertainties in signal are taken as fully correlated. The variables describing the background uncertainties are treated as uncorrelated between the two categories. The LP category contributes to the sensitivity of the analysis, especially at large values of m_{jj}. The combined expected limits on the $G_{\text{RS}} \to WW$ production cross sections are, respectively, a factor of 1.1 and 1.6 smaller at $m_{\text{jj}} = 1.0\text{TeVand}$ 2.9TeVthan the limit obtained from the HP category alone.

Figures 3.43 and 3.44 show the observed and background-only expected upper limits on the production cross sections for singly and doubly W/Z-tagged events,

Figure 3.43: Expected and observed 95% CL limits on the production cross section as a function of the resonance mass for (upper left) qW resonances, (upper right) qZ resonances, and (bottom) WZ resonances, compared to their predicted cross sections for the corresponding benchmark models.

computed at 95% CL, with the predicted cross sections for the benchmark models overlaid for comparison. Table 3.7 shows the resulting exclusion ranges on resonant masses. Compared to the previous search in this channel at $\sqrt{s} = 7\text{TeV}$ [18], the mass limits on $q* \to qW$ and $q* \to qZ$ are increased, respectively, by 0.8 and 0.7 TeVand
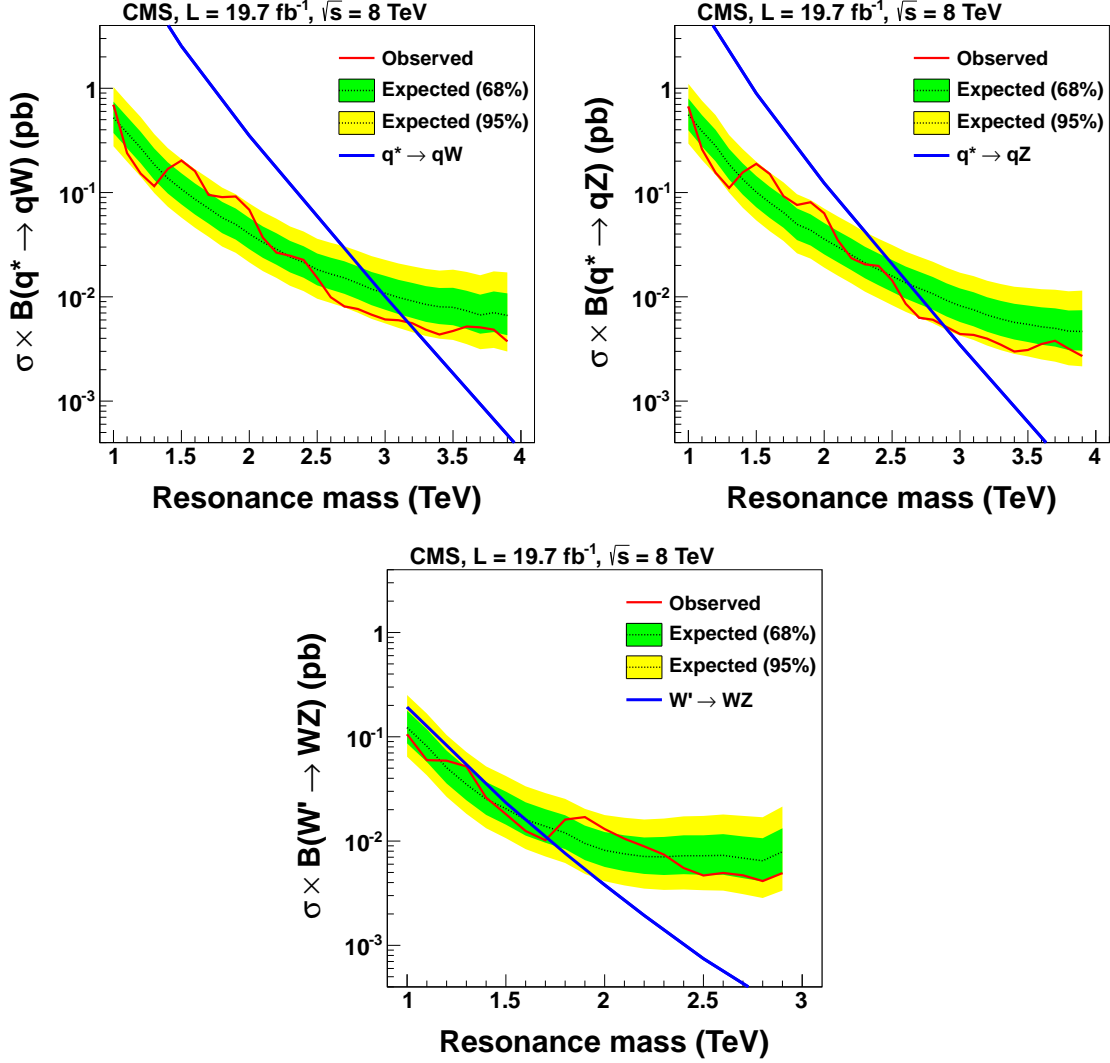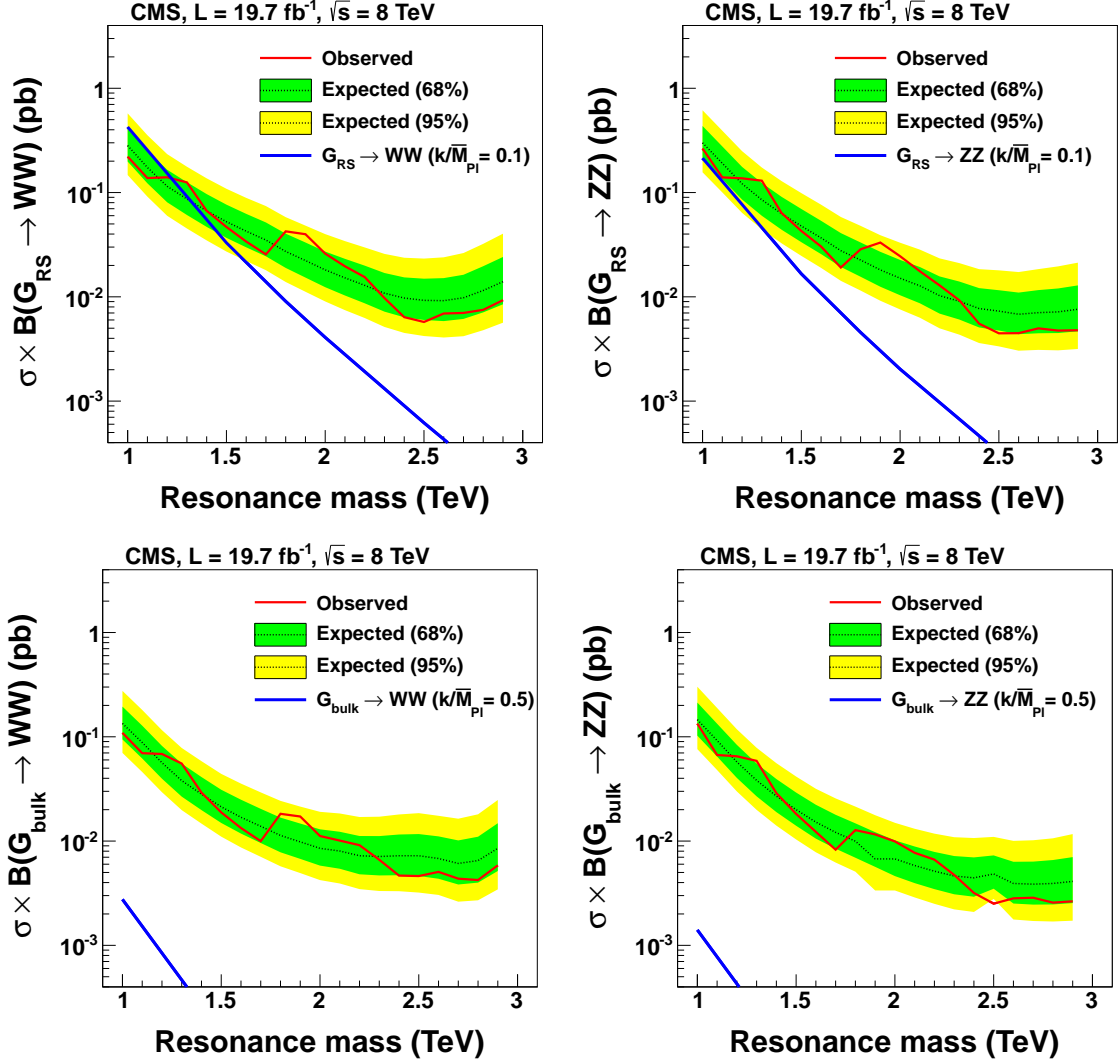
Figure 3.44: Expected and observed 95% CL limits on the production cross section as a function of the resonance mass for (upper left) $G_{\text{RS}} \to WW$ resonances, (upper right) $G_{\text{RS}} \to ZZ$ resonances, (bottom left) $G_{\text{Bulk}} \to WW$ resonances, and (bottom right) $G_{\text{Bulk}} \to ZZ$ resonances, compared to the predicted cross sections.

for the first time mass limits are set on $W' \to WZ$ and $G_{\text{RS}} \to WW$ models. No mass limits are set on $G_{\text{RS}} \to ZZ$, $G_{\text{Bulk}} \to WW$ and $G_{\text{Bulk}} \to ZZ$, since the analysis is not sensitive to the small predicted cross sections.

The systematic uncertainties have minor impact on the limits. The largest contri-

butions are 5%, 5%, and 3% from W/Z-tagging efficiency, JES, and JER, respectively.

These numbers are obtained by quoting the largest change in the observed exclusion

limit on the $G_{\mathrm{RS}} \to WW$ production cross section, over the entire examined mass

range, when the corresponding uncertainties are removed.

Table 3.7: Summary of observed limits on resonance masses at 95% CL and their expected values, assuming a null hypothesis. The analysis is sensitive to resonances heavier than 1TeV.

Process	Observed	Expected
	excluded mass limit (TeV)	excluded mass limit (TeV)
$q* \to qW$	3.2	3.0
$q* \to qZ$	2.9	2.6
$W' \to WZ$	1.7	1.6
$G_{\mathrm{RS}} \to WW$	1.2	1.3

3.12   Conclusions

A data sample corresponding to an integrated luminosity of 19.7 fb^{-1}collected in pp collisions at $\sqrt{s} = 8$TeVwith the CMS detector has been used to measure the W/Z-tagged dijet mass spectrum using the two leading jets within the pseudorapidity range $|\eta| < 2.5$ and with pseudorapidity separation $|\Delta\eta| < 1.3$. The QCD background is suppressed using jet substructure tagging techniques, which identify vector bosons decaying into hadrons. In particular, we use the invariant mass of pruned jets and the N-subjettiness ratio τ_{21} to discriminate against the initially overwhelming QCD background. The remaining QCD background is estimated from a fit to the smooth parameterized shape. We have searched for the signal as a peak on top of the smoothly falling QCD background. No evidence has been found for new resonance production in the W/Z-tagged dijet spectrum. A 95% CL lower limit is set on the mass of excited quark resonances decaying into qW (qZ) at 3.17 (2.88) TeV. G_{RS} decaying into WW is excluded up to 1.24 TeV. W' decaying into WZ is excluded in the ranges $[1.00, 1.23]$, $[1.39, 1.52]$ and $[1.57, 1.61]$ TeV.

Bibliography

[1] S.L.Glashow, *Nuclear Physics*, vol. 22, 1961.

[2] A.Salam, *Physics Review*, vol. 127, 1962.

[3] S. Weinberg, *Physics Review Letter*, vol. 19, 1967.

[4] C.Quigg, *Gauge Field Theories*. McGraw-Hill Book Company, 1983.

[5] Wikipedia, "Standard model," http://en.wikipedia.org/wiki/Standard_Model.

[6] David Griffiths, *Introduction to Elementary Particles*. Wiley-VCH Verlg GmbH & Co.KGaA, 2008.

[7] M. Belloni, "qcd confinement illustration," http://www.phy.davidson.edu/FacHome/mjb/images/color_field.gif.

[8] NASA, "The accelerated expansion of universe," http://science.nasa.gov/astrophysics/focus-areas/what-is-dark-energy/.

[9] Quantum Diaries, "The hierarchy problem: why the higgs has a

snowballs chance in hell," http://www.quantumdiaries.org/2012/07/01/ the-hierarchy-problem-why-the-higgs-has-a-snowballs-chance-in-hell/.

[10] LHC Collaboration, "The overview of lhc," http://www.atlas.ch/photos/atlas_ photos/selected-photos/detector-site/surface/.

[11] Wikipedia, "Pseudorapidity," http://en.wikipedia.org/wiki/Pseudorapidity.

[12] CMS Collaboration, *Physics TDR Vol 1. Detector Performance and Software*, 2006.

[13] ——, "Scheme of a drift tube," http://www.pd.infn.it/~conti/cms/ mycosmictest.html.

[14] CMS Collaboration, "Scheme of the carbon strip chamber," http://cms.web. cern.ch/news/cathode-strip-chambers.

[15] M. Gouzevitch, A. Oliveira, J. Rojo, R. Rosenfeld, G. Salam *et al.*, "Scale-invariant resonance tagging in multijet events and new physics in Higgs pair production," 2013.

[16] CMS Collaboration, "Study of jet substructure in pp collisions at 7 TeV in CMS," CMS Physics Analysis Summary CMS-PAS-JME-10-013, 2010. [Online]. Available: http://cdsweb.cern.ch/record/1333700

[17] ——, "Identifying hadronically decaying vector bosons merged into a single

jet," CMS Physics Analysis Summary CMS-PAS-JME-13-006, 2013. [Online]. Available: http://cdsweb.cern.ch/record/1598864

[18] ——, "Search for heavy resonances in the w/z-tagged dijet mass spectrum in pp collisions at 7 tev," *Phys. Lett. B*, vol. 723, p. 280, 2013.

[19] J. Thaler and K. Van Tilburg, "Identifying Boosted Objects with N-subjettiness," *JHEP*, vol. 1103, p. 015, 2011.

[20] U. Baur, I. Hinchliffe, and D. Zeppenfeld, "Excited quark production at hadron colliders," *Int. J. Mod. Phys. A*, vol. 2, p. 1285, 1987.

[21] U. Baur, M. Spira, and P. M. Zerwas, "Excited-quark and -lepton production at hadron colliders," *Phys. Rev. D*, vol. 42, p. 815, 1990.

[22] L. Randall and R. Sundrum, "A large mass hierarchy from a small extra dimension," *Phys. Rev. Lett.*, vol. 83, p. 3370, 1999.

[23] ——, "An alternative to compactification," *Phys. Rev. Lett.*, vol. 83, p. 4690, 1999.

[24] K. Agashe, H. Davoudiasl, G. Perez, and A. Soni, "Warped gravitons at the LHC and beyond," *Phys. Rev. D*, vol. 76, p. 036006, 2007.

[25] O. Antipin, D. Atwood, and A. Soni, "Search for RS gravitons via $w_l w_l$ decays," *Phys. Lett. B*, vol. 666, p. 155, 2008.

[26] O. Antipin and A. Soni, "Towards establishing the spin of warped gravitons," *JHEP*, vol. 10, p. 018, 2008.

[27] G. Altarelli, B. Mele, and M. Ruiz-Altaba, "Searching for new heavy vector bosons in $p\bar{p}$ colliders," *Z. Phys. C*, vol. 45, p. 109, 1989, erratum-ibid. C **47** (1990) 676.

[28] CMS Collaboration, "Search for narrow resonances using the dijet mass spectrum in pp collisions at $\sqrt{s} = 8$ TeV," 2012, submitted to Phys. Rev. Lett.

[29] ATLAS Collaboration, "Atlas search for new phenomena in dijet mass and angular distributions using pp collisions at $\sqrt{s} = 7$ TeV," *JHEP*, vol. 1301, p. 029, 2013.

[30] R. M. Harris and K. Kousouris, "Searches for Dijet Resonances at Hadron Colliders," *Int.J.Mod.Phys.*, vol. A26, pp. 5005–5055, 2011.

[31] F. Abe *et al.*, "Search for excited quarks in $p\bar{p}$ collisions at $\sqrt{s} = 1.8$ TeV," *Phys. Rev. Lett.*, vol. 72, p. 3004, 1994.

[32] V. M. Abazov *et al.*, "Search for a heavy resonance decaying into a Z+ jet final state in p$\bar{p}$ collisions at $\sqrt{s} = 1.96$ TeV using the D0 detector," *Phys. Rev. D*, vol. 74, p. 011104, 2006.

[33] CMS Collaboration, "Search for anomalous production of highly boosted Z

bosons decaying to dimuons in pp collisions at $\sqrt{s} = 7$ TeV," *Phys. Lett. B,* vol. 722, p. 28, 2013.

[34] ——, "Search for a narrow spin-2 resonance decaying to a pair of Z vector bosons in the semileptonic final state," *Phys. Lett. B,* vol. 718, p. 1208, 2013.

[35] G. Aad *et al.,* "Search for resonant diboson production in the ww/wz $\rightarrow l\nu jj$ decay channels with the atlas detector at $\sqrt{s} = 7$ TeV," *Phys. Rev. D,* vol. 87, p. 112006, 2013.

[36] ——, "Search for new particles decaying to ZZ using final states with leptons and jets with the ATLAS detector in $\sqrt{s} = 7$ TeV proton-proton collisions," *Phys. Lett. B,* vol. 712, p. 331, 2012.

[37] T. Aaltonen *et al.,* "Search for high-mass resonances decaying into ZZ in p$\bar{p}$ collisions at $\sqrt{s} = 1.96$ TeV," *Phys. Rev. D,* vol. 85, p. 012008, 2012.

[38] S. Chatrchyan *et al.,* "Search for new physics in final states with a lepton and missing transverse energy in pp collisions at the lhc," *Phys. Rev. D,* vol. 87, p. 072005, 2013.

[39] G. Aad *et al.,* "Search for a heavy gauge boson decaying to a charged lepton and a neutrino in 1 fb^{-1} of pp collisions at $\sqrt{s} = 7$ TeV using the ATLAS detector," *Phys. Lett. B,* vol. 705, p. 28, 2011.

[40] ——, "Search for resonant WZ production in the WZ to l nu l' l' channel in

$\sqrt{s} = 7$ TeV pp collisions with the ATLAS detector," *Phys. Rev. D*, vol. 85, p. 112012, 2012.

[41] CMS Collaboration, "Particle–flow event reconstruction in CMS and performance for jets, taus, and E_T^{miss}," CMS Physics Analysis Summary CMS-PAS-PFT-09-001, 2009. [Online]. Available: http://cdsweb.cern.ch/record/1194487

[42] M. Wobisch and T. Wengler, "Hadronization corrections to jet cross sections in deep-inelastic scattering," 1998.

[43] Y. L. Dokshitzer, G. D. Leder, S. Moretti, and B. R. Webber, "Better jet clustering algorithms," *JHEP*, vol. 08, p. 001, 1997.

[44] M. Cacciari and G. P. Salam, "Dispelling the N**3 myth for the k(t) jet-finder," *Phys. Lett. B*, vol. 641, p. 57, 2006.

[45] M. Cacciari, G. P. Salam, and G. Soyez, "Fastjet user manual," *Eur. Phys. J. C*, vol. 72, p. 1896, 2012.

[46] ——, "The catchment area of jets," *JHEP*, vol. 04, p. 005, 2008.

[47] M. Cacciari and G. P. Salam, "Pileup subtraction using jet areas," *Phys. Lett. B*, vol. 659, p. 119, 2008.

[48] CMS Collaboration, "Determination of Jet Energy Calibration and Transverse Momentum Resolution in CMS," *J. Instrum.*, vol. 6, p. P11002, 2011.

BIBLIOGRAPHY

[49] ——, "Jet energy corrections and uncertainties detector performance plots for 2012," *CMS Detector Performance Plots*, vol. DP-2012/012, 2012.

[50] Y. Gao, A. V. Gritsan, Z. Guo, K. Melnikov, M. Schulze *et al.*, "Spin determination of single-produced resonances at hadron colliders," *Phys.Rev.*, vol. D81, p. 075022, 2010.

[51] S. Bolognesi, Y. Gao, A. V. Gritsan, K. Melnikov, M. Schulze *et al.*, "On the spin and parity of a single-produced resonance at the LHC," *Phys.Rev.*, vol. D86, p. 095031, 2012.

[52] T. Sjöstrand, S. Mrenna, and P. Skands, "PYTHIA 6.4 physics and manual," *JHEP*, vol. 05, p. 026, 2006.

[53] S. Gieseke, M. A. Gigg, D. Grellscheid, K. Hamilton, O. Latunde-Dada, S. Plätzer, P. Richardson, M. H. Seymour, A. Sherstnev, and B. R. Webber, "Herwig++ 2.5 release note."

[54] S. Agostinelli *et al.*, "GEANT4—a simulation toolkit," *Nucl. Instrum. Meth. A*, vol. 506, p. 250, 2003.

[55] J. Pumplin, D. R. Stump, J. Huston, H.-L. Lai, P. Nadolsky, and W.-K. Tung, "New generation of parton distributions with uncertainties from global QCD analysis," *JHEP*, vol. 07, p. 012, 2002.

[56] A. D. Martin, R. G. Roberts, W. J. Stirling, and R. S. Throne, "MRST2001:

partons and alpha_s from precise deep inelastic scattering and tevatron jet data,"
Eur. Phys. J. C, vol. 23, p. 73, 2002.

[57] R. Field, "Early LHC underlying event data – findings and surprises," in *Proceeedings of the Hadron Collider Physics Symposium 2010*, 2010.

[58] CMS Collaboration, "Search for Randall-Sundrum graviton excitations in the CMS experiment," 2002.

[59] S. Chatrchyan, "Search for resonances in the dijet mass spectrum from 7 TeV pp collisions at CMS," *Phys. Lett. B*, vol. 704, p. 123, 2011.

[60] J. Alwall, P. Demin, S. de Visscher, R. Frederix, M. Herquet, F. Maltoni, T. Plehn, D. L. Rainwater, and T. Stelzer, "MadGraph 5: Going beyond," *JHEP*, 2011.

[61] CMS Collaboration, "Status of the 8 tev jet energy corrections and uncertainties based on 11/fb of data in cms," *CMS Detector Performance Plots*, vol. DP-2013/011, 2013.

[62] ——, "Cms luminosity based on pixel cluster counting - summer 2013 update," CMS Physics Analysis Summary CMS-PAS-LUM-13-001, 2013. [Online]. Available: http://cdsweb.cern.ch/record/1598864

[63] G. Cowan, K. Cranmer, E. Gross, O. Vitells, "Asymptotic formulae for likelihood based tests of new physics," *Eur. Phys. J.*, vol. C71, p. 1554, 2011.

[64] A. L. Read, "Presentation of search results: The CL(s) technique," *J. Phys.*, vol. G28, pp. 2693–2704, 2002.

[65] A. Read, "Modified frequentist analysis of search results (the CL_s method)," CERN, Tech. Rep. CERN-OPEN-2000-005, 2000. [Online]. Available: http://cdsweb.cern.ch/record/451614